Characterization of Irreversible Land Subsidence in the Yazd-Ardakan Plain, Iran from 2003-2020 InSAR Time Series

Sayyed Mohammad Javad Mirzadeh[1,2], Shuanggen Jin[1,3], Esmaeel Parizi[4], Estelle Chaussard[5,11], Roland Bürgmann[6], Jose Manuel Delgado Blasco[7], Meisam Amani[8], Han Bao[9], and Seyyed Hossein Mirzadeh[10]

[1]Shanghai Astronomical Observatory, Chinese Academy of Sciences, Shanghai 200030, China

[2]School of Astronomy and Space Science, University of Chinese Academy of Sciences, Beijing 100049, China

[3]School of Remote Sensing and Geomatics Engineering, Nanjing University of Information Science and Technology, Nanjing 210044, China

[4]Physical Geography Department, University of Tehran, P.O. Box 14155-6465, Tehran, Iran

[5]Department of Earth Sciences, University of Oregon, Eugene, OR, USA

[6]Department of Earth and Planetary Science, University of California Berkeley, Berkeley, CA 94720-4767, USA

[7]Grupo de Investigación Microgeodesia Jaén (PAIDI RNM-282), Universidad de Jaén, 23071 Jaén, Spain

[8]Wood Environment & Infrastructure Solutions, Ottawa, ON, Canada, K2E 7L5

[9]Earth, Planetary, and Space Sciences, University of California, Los Angeles, CA, USA

[10]Faculty of Architecture and Urban Planning, University of Art, Tehran 1136813518, Iran

[11] Currently unaffiliated

Corresponding author: sgjin@shao.ac.cn; sg.jin@yahoo.com (S. Jin)

Key Points:

- Vertical and horizontal deformation in Yazd-Ardakan Plain, Iran, is obtained by Envisat and Sentinel-1 InSAR time series
- The rates and spatial extent of subsidence are controlled by the confining clay layer thickness
- An Independent Component Analysis shows that the subsidence is irreversible and inelastic compaction dominates

Abstract

Groundwater extraction at rates exceeding recharge is occurring throughout Iran for agricultural and industrial activities, resulting in land subsidence in many areas, particularly the Yazd-Ardakan Plain (YAP) in the dry and desert regions of central Iran. In this study, Interferometric Synthetic Aperture Radar (InSAR) time series analysis and statistical models are used to characterize the controls on land subsidence in the YAP, from 2003 to 2020. Our results reveal the existence of a northwest-southeast elongated area of 363 km^2 experiencing subsidence at rates up to 15 cm/yr. In the YAP, the international Airport, railway, transit road, and several industrial and historical sites are threatened by the differential subsidence. Well data confirm that groundwater levels have decreased by 18 meters between 1974 and 2018, driving the compaction of sediments within the underlying aquifer system. Our statistical analysis shows that the thickness of a shallow, clay-rich aquitard layer controls the extent of the observed subsidence and an Independent Component Analysis of the InSAR time series shows that inelastic compaction dominates. This work reveals that in central Iran, current groundwater extraction practices are not sustainable and result in permanent subsidence, ground fractures with impact on infrastructures, and a permanent decrease in water storage capacity.

1 Introduction

Deserts and semi-deserts currently occupy more than one-third of the global land surface (Laity, 2009). In these areas, recent climatic changes (i.e. increasing temperature and decreasing precipitation) occur at a faster rate than in other environments (Porter et al., 2014). These changes result in the loss of valuable topsoil by wind erosion, soil salinization, loss of sparse vegetation, and dropping groundwater levels (Laity, 2009). In addition, the population growth and industrial and urban developments in desert areas have resulted in increasing exploitation of underground water resources (Avtar et al., 2019), which leads to land subsidence. Land subsidence is well-known in desert and semi-desert areas such as the Las Vegas Valley, Nevada, USA (Amelung et al., 1999), the Avra Valley, Arizona, USA (Hanson et al., 1990), the Mojave Desert, California, USA (Galloway et al., 1998), in Mexico's San Luis Potosı´ state and Mexico City (Chaussard et al., 2021; Julio-Miranda et al., 2012), in the South Kordofan state, Sudan (Gido et al., 2020), in areas of Saudi Arabia (Amin and Bankher, 1997), and in the Kerman and Yazd regions of Iran (Motagh et al., 2008). Several environmental effects are associated with land subsidence, including damage to infrastructure and buildings, accelerated erosion along earth fissures, drainage systems, degradation and contamination of groundwater, and socio-economic impacts (Abidin et al., 2001; Chaussard et al., 2021; Conway, 2016). Therefore, it is important to monitor and investigate both the temporal variability and spatial extent of land subsidence to establish a continuous monitoring system and to assist in the development of a sustainable water management program (Baum et al., 2008; Emil et al., 2018).

Although ground-based geodetic surveys such as precise differential leveling and Global Navigation Satellite System (GNSS) positioning (Jin and Su, 2020) are accurate techniques for monitoring land subsidence, these approaches are time-consuming and costly and thus spatially limited (Galloway and Burbey, 2011). Remote sensing techniques can be used to map and measure the subcentimeter ground displacement at high spatial resolution (tens to hundreds meters) over large areas (tens to thousands of square kilometers), and are thus well suited for monitoring land subsidence (e.g. Chaussard et al. (2013); Chaussard et al. (2014b)). Interferometric synthetic aperture radar (InSAR) enables quantifying surface topography and its changes over large regions (Bürgmann et al., 2000). InSAR uses several Synthetic Aperture Radar (SAR) images of the same area acquired at different times by a single antenna or at the same time by two antennas separated in an along-track direction. InSAR has offered insights into

the hydrogeological and geological processes in deforming aquifers (Bell et al., 2008; Bozzano et al., 2015; Chaussard et al., 2017; Hoffmann et al., 2001; Hu et al., 2018; Ojha et al., 2018; Schmidt and Bürgmann, 2003).

In Iran, intense irrigation of agricultural areas, industrial needs, and rapid urban development are the main sources of groundwater over-drafting and cause the resulting depletion of water reservoirs (e.g., Anderssohn et al. (2008)). Throughout the country, the volume of annual groundwater extraction increased from 20 billion m^3 in 1960 to more than 53 billion m^3 in 2003 (World Bank, 2005). Land subsidence is documented in more than 300 plains or sedimentary basins of Iran (Amighpey and Arabi, 2016; Anderssohn et al., 2008; Babaee et al., 2020). For example, Motagh et al. (2017) explored land subsidence in the Rafsanjan plain through InSAR time series analysis using Envisat, ALOS-1, and Sentinel-1 datasets between 2004 and 2016. Their study showed subsidence exceeding 30 cm/yr. Haghighi and Motagh (2019) reported three distinct subsidence features with rates up to 25 cm/yr in the capital of Iran, Tehran, using 2003-2017 time series analysis of the Envisat, TerraSAR-X, ALOS, and Sentinel-1 data, and showed that inelastic (permanent) compaction dominated in this aquifer.

The Yazd-Ardakan Plain (YAP) is one of the main strategic regions in Iran in terms of aggregation of infrastructures, industrial sites, and transportation corridors (Fig. 1, Table S2) (Esfanjary, 2018). Increasing demand for water resources in recent decades, due to population growth and industrial and agricultural developments, has led to groundwater depletion and subsidence (Amighpey and Arabi, 2016). In this study, we quantify the spatiotemporal evolution of land subsidence in the YAP using InSAR time series analysis to resolve the underlying controls on subsidence rates and spatial extent. The Small BAseline Subset (SBAS) time series technique (Berardino et al., 2002; Hooper, 2008) was implemented using both the Envisat and Sentinel-1 datasets to derive time-dependent subsidence between 2003 and 2020. InSAR time series results were then analyzed with an Independent Component Analysis (ICA) to separate contributions from elastic (i.e., reversible) and inelastic (i.e. irreversible) deformation (Chaussard and Farr, 2019). Finally, hydrogeological and geological parameters were combined using statistical and artificial intelligence (AI) methods to quantify the dominant control on the observed deformation in the YAP aquifer.

2 Yazd-Ardakan Plain

The Yazd-Ardakan Plain (YAP) is located between 53.65 and 54.77 E longitude and 31.55 and 32.50 N latitude in the central part of the province of Yazd (Fig. 1). The elevation in this region rises from 997 m to 2677 m above sea level from the north towards the south.

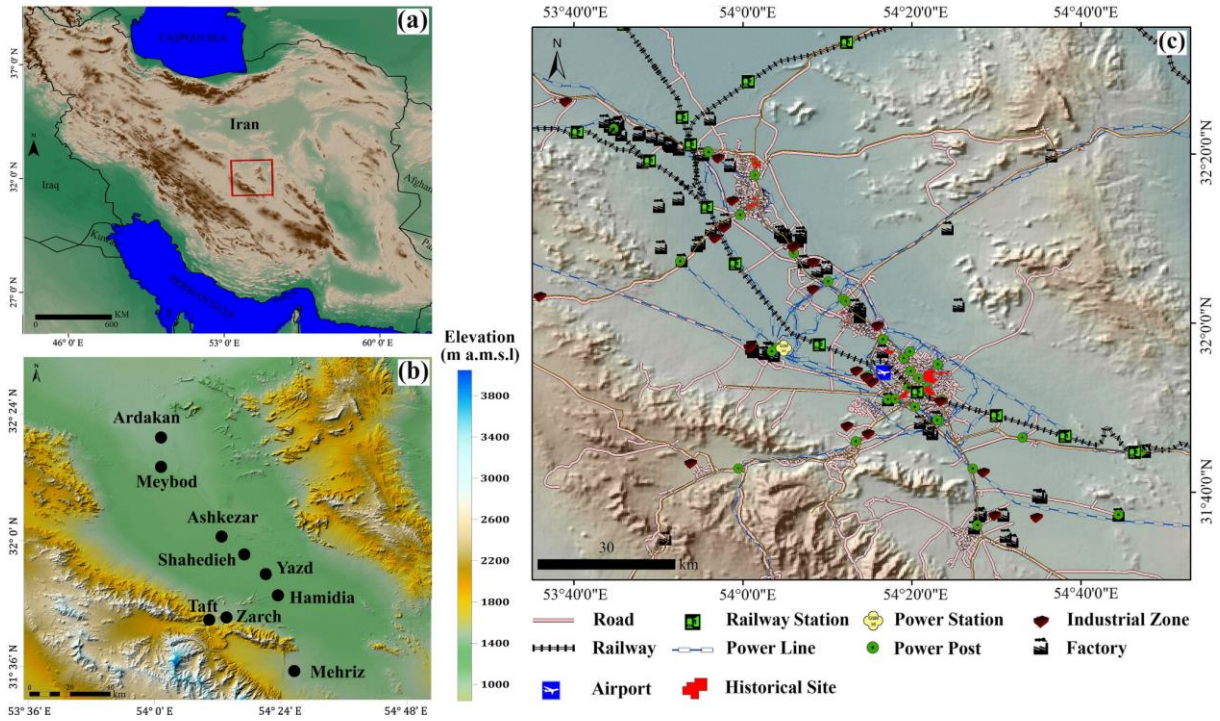

Figure 1. (a) Location of Yazd-Ardakan Plain (YAP) in Iran, indicated with a red rectangle. (b) Topography of the YAP with black dots showing the cities of Ardakan, Meybod, Ashkezar, Shahedieh, Yazd, Hamidia, Zarch, Taft, and Mehriz. (c) Main infrastructures, industrial and historical sites located in the YAP (see Table S2).

The YAP is a dry desert with average annual evaporation of ~ 2900 mm and average annual rainfall of ~ 130 mm (TAMAB, 2004) based on recorded data during 1969 to 2011. Within the YAP, there is no year-round surface water and, accordingly, cities have relied on groundwater delivered through qanats (a system of connected underground wells). The YAP aquifer covers an area of 2618.57 km^2 (Fig. 2a). This confined aquifer is topped by a tens-of-meters thick clay-rich aquitard layer in the central part of the valley (light-blue in Fig. 2b). Groundwater levels are measured monthly by the Iran Water Resources Management (TAMAB, 2004) using 81 piezometers, which reveal maximum and minimum depths to water levels of 164.6 m and 8.12 m, respectively (Regional Water Company of Yazd, 2014). Approximately 282

142 million m^3 of groundwater are being extracted annually from 1194 pumping wells, leading to a
143 net storage loss of ~ 65.93 million m^3 per year (TAMAB, 2004). This large net storage loss has
144 led the Water Resource Company of Ministry of Energy to label the YAP as a "forbidden"
145 aquifer, a term used to refer to the most imperiled aquifers in Iran (Regional Water Company of
146 Yazd, 2014). Table S1 provides the discharge and recharge components of the groundwater
147 balance of the YAP, which shows that the primary source of aquifer discharge is withdrawal
148 through wells, qanats, and springs at 323.14 million m^3 per year (Fig. S1). A key contribution to
149 aquifer recharge comes from return of wastewater from the agricultural sector at 84.14 million
150 m^3 per year, while recharge by precipitation amounts to only 11.53 million m^3 per year and loss
151 by evaporation from groundwater was estimated to be insignificant (Regional Water Company of
152 Yazd, 2014).

153 Figure 2a shows the Jurassic to Quaternary lithologies observed in the YAP. Quaternary
154 sediments cover the largest part of the YAP with 74.6% of this area, consisting of sand dunes,
155 alluvium, and sabkha (salty silts, clays, and salt flats). The Dehshir fault, a 400 km-long NNW-
156 trend strike-slip fault (Walker and Jackson, 2004) with an estimated right-lateral slip rate of 2
157 mm per year (Walker et al., 2009), is bounding the YAP to the southwest (red line on Fig. 2a).
158

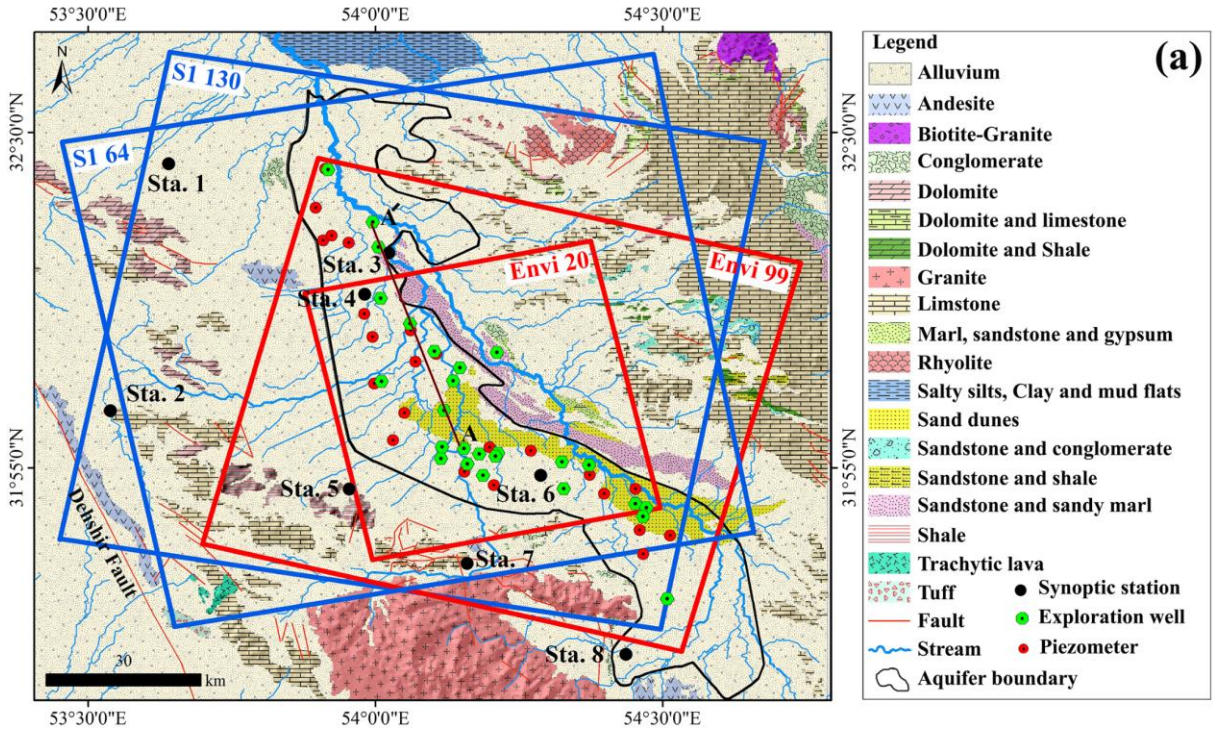

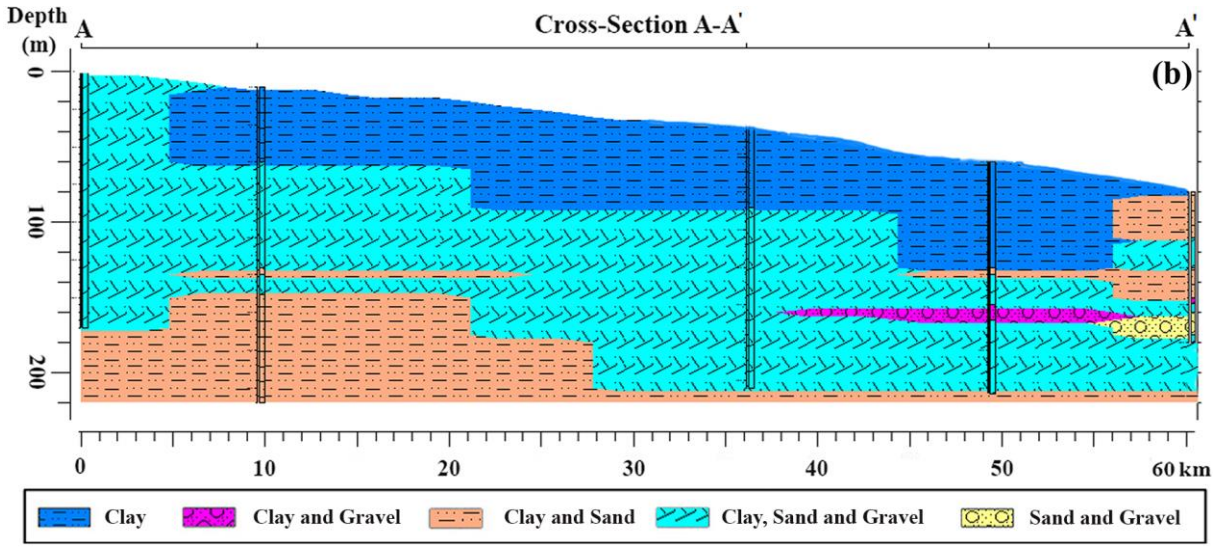

Figure 2. (a) Geological map of the YAP, modified from the Geological Survey of Iran (1997). Black lines represent the confined aquifer boundary. Brown lines show the locations of cross-sections (A-A' and B-B'). Red and green dots show the locations of piezometers and exploration wells, respectively. Black dots, labeled by Sta.1 to Sta. 8, show the location of synoptic stations, Aqda, NasrAbad, Ardakan, Meybod, Sadoogh, Yazd, Taft, and Mehriz. Outline of frames from Sentinel-1 and Envisat tracks in the ascending and descending orbit directions are shown with the blue and red rectangles, respectively. (b) Geologic cross-section of the YAP aquifer along the A-A' relying on data from the exploration wells shown in (a). They show that the geological materials of the aquifer are mostly unconsolidated sediments (clay and sand: orange; sand and gravel: yellow; clay, sand, and gravel mix: cyan; and gravel and clay: purple), and their thickness decreases from the south (left) to the north (right). The thickness of the topmost clay unit (blue) represents the confining aquitard layer.

3 Datasets and Methods

3.1 Datasets

3.1.1 SAR satellite data

We used 248 Sentinel-1 images acquired in Interferometric Wide-swath (IW) mode, from the Alaska Satellite Facility (ASF), and 40 Envisat ASAR images in StripMap (SM) mode from the European Space Agency (ESA). Sentinel-1 images were acquired from October 2014 to March 2020 from both descending and ascending orbits (Fig. 2a) with a resolution of 5 × 20 m (Range × Azimuth). The Envisat ASAR images were acquired from March 2003 to October 2010 and from September 2004 to July 2010 from the descending and ascending orbits, respectively (Fig. 2a), with a spatial resolution of 8 × 4 m (Range × Azimuth).

3.1.2 Hydrological data

We used monthly data from 23 piezometers to assess groundwater level (GWL) variations between 2004 and 2018 (Fig. 2a). We used an Inverse Distance Weighted (IDW) (ESRI, 2012; Gong et al., 2014) approach to produce a map of annual GWL changes (Fig. S4c). The Kernel Density method (Trabelsi et al., 2016) was used to map the density of pumping wells (Fig. S4b) and annual pumping volume (Fig. S4d) by interpolation of 1194 pumping wells data (Fig. S4f). Aquifer transmissivity is one of the most important variables affecting yields of a pumping well. It is equal to the product of the aquifer thickness (m) and hydraulic conductivity (K) and describes an aquifer's capacity to transmit water (Cheremisinoff, 1998; Sterrett, 2007). A transmissivity map (Fig. S4e) was generated by interpolation of transmissivity point data from the pumping test (Parizi et al., 2019; Regional Water Company of Yazd, 2014).

3.1.3 Geological data

Stratigraphic data within the YAP (Fig. 2a) is derived from the geological map at a scale of 1:100000, provided by the Geological Survey and Mineral Explorations of Iran (GSI) (Geological Survey of Iran, 1997). The logs of 26 exploration wells (Fig. 2a; TAMAB (2004)), were utilized to derive the spatial distribution and thickness of clay sediments (Fig. S4a) with an Inverse Distance Weighted (IDW) approach (ESRI, 2012; Gong et al., 2014).

3.1.4 Weather data

Time-series of Land Surface Temperature (LST) were generated using the MODIS/Terra product MOD11_L2 swath that provides daily LST and emissivity values with a resolution of 1 km in a 1200 km × 1200 km grid. Time series of precipitation were generated using the daily precipitation data of eight stations (see their locations in Fig. 2a), distributed in the YAP (Iran Meteorological Organization, 2018). The Temperature-Vegetation-soil Moisture Dryness Index (TVMDI) was computed using (1) LST data, (2) Soil Moisture (SM) data, and (3) Perpendicular Vegetation Index (PVI) in the form of TVMDI = $\sqrt{LST^2 + SM^2 + (\frac{\sqrt{3}}{3} - PVI)^2}$, used to assess the pattern of dryness over the study area (Amani et al., 2017).

196 ## 3.2 Methods

197 ### 3.2.1 InSAR processing

198 The InSAR Computing Environment (ISCE) software was used to produce over 970 and
199 280 Sentinel-1 and Envisat interferograms, respectively (see Fig. 3). Temporal and perpendicular
200 baseline thresholds were set to 1800 days and 1070 m for the Envisat data. For Sentinel-1 data,
201 interferograms were formed between each epoch and the four preceding and four subsequent
202 epochs. To reduce the speckle noise and increase processing speed, the interferograms were
203 resampled to ~ 90 m and ~ 30 m for the Envisat and Sentinel-1 datasets, respectively. The
204 topographic phase was removed using the 1-arcsec Shuttle Radar Topography Mission (SRTM)
205 Digital Elevation Model (DEM) (Jarvis et al., 2008). The statistical-Cost Network-Flow
206 Algorithm for Phase Unwrapping (SNAPHU) was used for phase unwrapping (Chen and Zebker,
207 2003). As deformation rates before and after large data gaps in 2007 were consistent, a joint rate
208 (linear fit + offset) was calculated for the descending Envisat dataset (Fig. S3). A similar
209 approach was also used to combine the individual Envisat time series into a single time series,
210 assuming constant subsidence rates, as suggested by individual time series.

211 We used the Small BAseline Subset (SBAS) time series method (Berardino et al., 2002)
212 implemented in the Miami INsar Time-series software in PYthon (MintPy) (Yunjun et al., 2019)
213 to invert a network of interferograms and retrieve surface displacement through time. In MintPy,
214 average spatial coherence thresholds of 0.87 and 0.77 (Fig. 3) were used to remove outliers
215 affected by unwrapping errors (Tizzani et al., 2007) for the Envisat ascending and descending,
216 respectively. The tropospheric delay was corrected using PyAPS (Jolivet et al., 2014; Jolivet et
217 al., 2011) and the ECMWF Reanalysis v5 (ERA-5) weather model with a spatial resolution of 31
218 km (Hersbach et al., 2020). Regional phase ramps caused by long-wavelength tropospheric and
219 ionospheric delays and orbital errors were removed by a linear ramp calculated at each
220 acquisition. The empirical model of Marinkovic and Larsen (2013) was used to correct the Local
221 Oscillator Drift (LOD) of the ASAR instrument and to improve the geo-location accuracy of the
222 Envisat interferograms. Finally, the displacement time series were all referenced to a single pixel
223 that exhibits high coherence (cross in Fig. 5).
224

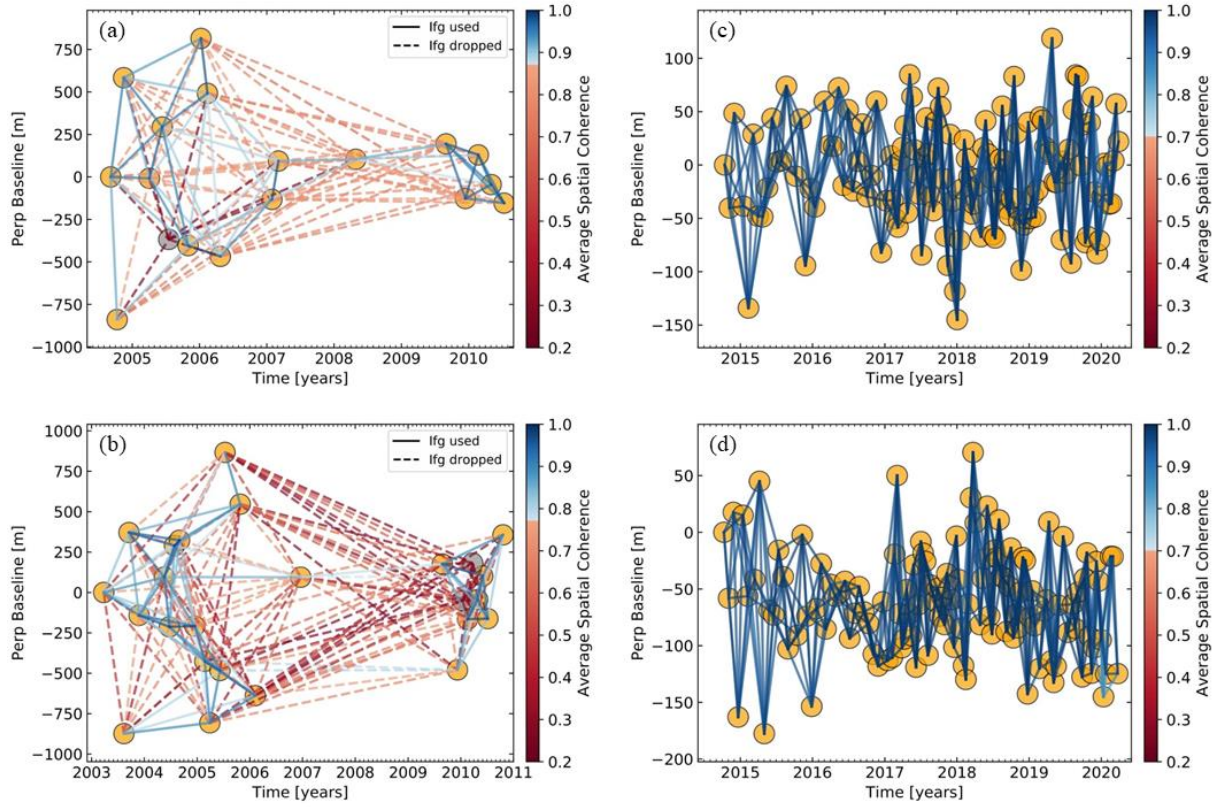

Figure 3. Envisat and Sentinel-1 interferograms visualized in the spatial and temporal baseline domains and color-coded by average spatial coherence. (a) Envisat ascending, (b) Envisat descending, (c) Sentinel-1 ascending, and (d) Sentinel-1 descending. Dashed lines in (a) and (b) illustrate Envisat interferograms dropped when applying the average spatial coherence thresholds. Solid lines show interferograms inverted to retrieve the time series of surface deformation.

Ascending and descending time series were combined to calculate the vertical and east-west components, assuming no contributions from the north-south component (Wright et al., 2004), by minimizing

$$\begin{bmatrix} v_e \\ v_u \end{bmatrix} = U \cdot \begin{bmatrix} d_e \\ d_u \end{bmatrix} - R_{LOS}$$

where $d = (d_e, d_u)^T$ is the 2D deformation vector (east-west, vertical); (v_e, v_u) are the observation residuals, and $U = \begin{bmatrix} \sin(\theta_A) \cdot \cos(\emptyset_A) & \cos(\theta_A) \\ \sin(\theta_D) \cdot \cos(\emptyset_D) & \cos(\theta_D) \end{bmatrix}$ is a matrix, including the Line-Of-Sight (LOS) vectors, where θ is the incident angle value for each Distributed Scatterer (DS) and $\emptyset$ is the satellite-heading angle for each orbit. R_{LOS} contains the LOS measurements for the ascending and descending orbits. If the covariance matrix for errors in the LOS measurements is

Σ_R, by minimizing the observation residuals, the deformation vector $d = -(U^T.\Sigma_R^{-1}.U)^{-1}.U^T.\Sigma_R^{-1}.R$ can be calculated with a weighted least-squares inversion. The covariance matrix for the vector components is $\Sigma_d = (U^T.\Sigma_R^{-1}.U)^{-1}$ and, as errors in LOS measurements are independent in the ascending and descending measurements, we get

$$\Sigma_d = \sigma^2(U^T.U)^{-1}$$

where $\sigma^2 = \begin{bmatrix} \sigma_A^2 & 0 \\ 0 & \sigma_D^2 \end{bmatrix}$; and σ_A^2 and σ_D^2 are the standard deviations for the ascending and descending orbits, respectively. The square root of the diagonal terms of Σ_d gives a standard displacement errors that can be considered as uncertainties in space over the YAP. InSAR uncertainties in time were calculated by averaging a 31x31 pixels window near the reference point at each time step of the ascending and descending time series for both the Envisat and Sentinel-1 datasets.

3.2.2 GWL changes and ground displacement

To assess the potential relationship between the GWL changes and the observed deformation, we gather time series of vertical displacement and of GWL at the locations of piezometers. To generate time series of vertical displacement from the LOS Sentinel-1 ascending and descending time series, we calculate the pixel-wise horizontal-to-vertical ratios from the mean horizontal and vertical velocity maps and multiplied the LOS deformation at each pixel by the corresponding ratio (assuming that the ratio of horizontal-to-vertical displacement at each pixel is constant throughout the Sentinel-1 observation period). During the period of record, converted-vertical displacements are computed in two-week intervals while the GWL change are only available monthly. Due to this temporal sampling difference, we choose to compare duration curves of converted-vertical displacements to GWL changes.

A duration curve illustrates the data variability in the frequency domain by illuminating the proportion of the data that exceeds the given value of data. Duration curves are widely used to characterize the streamflow variability over different time steps (e.g., daily, monthly, and yearly) (Castellarin et al., 2004; Ghotbi et al., 2020a; Ghotbi et al., 2020b; Vogel and Fennessey, 1994). The duration curves of GWL changes and vertical displacement (referred to hereafter as GDC for Groundwater Duration Curves and DDC for Displacement Duration Curves, respectively) are computed from the 2014-2018 data. For computing the GDC, monthly GWL changes are sorted in decreasing order and are each attributed a rank (e.g. rank m = 1,2, …, n)

with the rank n corresponding the smallest GWL change. The probability of the ranked GWL change (i.e., GWL_i where i = 1, 2, …, n) is a probability that GWL is greater than the given ranked value (GWL_i), and is computed with the Weibull method i.e., $P_i = \frac{m}{n+1}$ (Vogel and Fennessey, 1994). The GDC shows GWL_i as a function of P_i with the central part of duration curves (i.e., 30th to 70th percentiles) representing the long-term variability (Sawicz et al., 2011) while other parts of duration curves are related to the high and low variabilities of the GWL changes and vertical displacement. As such, to quantify the long-term variability from duration curves, we compute the corresponding slope S_{DC} (Yadav et al., 2007):

$$S_{DC} = \frac{Y_{30\%} - Y_{70\%}}{0.70 - 0.30}$$

where $Y_{30\%}$ and $Y_{70\%}$ are the values (e.g., GWL_{30} and GWL_{70} GWL or D_{30} and D_{70}), corresponding to the 30rd and 70th percentiles of exceedance probability, respectively.

3.2.3 Statistical modeling methods

To explore the controls on the land subsidence rates and extent, we compare the observed deformation to deformation simulated from potential predictor variables (clay layer thickness, density of pumping wells, GWL changes, annual pumping volume, and transmissivity; Fig. 4; (SHIBASAKI, 1969)) through (1) a Multi-Linear Regression (MLR) approach and (2) a Support Vector Machine Regression (SVR) (Abdollahi et al., 2019; Tien Bui et al., 2018; Vapnik, 1995) approach. A MLR, with Y and X_i , representing the observed response (land subsidence) and the potential predictor variables, respectively, and a_0 a regression constant and a_i the coefficients of the model follows:

$$Y = a_0 + a_1 \times X_1 + a_2 \times X_2 + \ldots + a_i \times X_i$$

We use the Statistics and Machine Learning Toolbox of MathWorks and a linear epsilon-insensitive SVR (ε-SVR) approach, also known as $L1$ loss (MathWorks, 2019). In ε-SVR, training data include the values of potential predictor variables and the observed response (Fig. 4) with the goal of finding a function $f(x)$ which can be linear, quadratic, cubic, fine-gaussian, medium-gaussian, or coarse-gaussian (MathWorks, 2019) that deviates from the observed response values (y_n) by a value no greater than ε for a multivariate set of the potential predictor variables (x_n) (Chen et al., 2006).

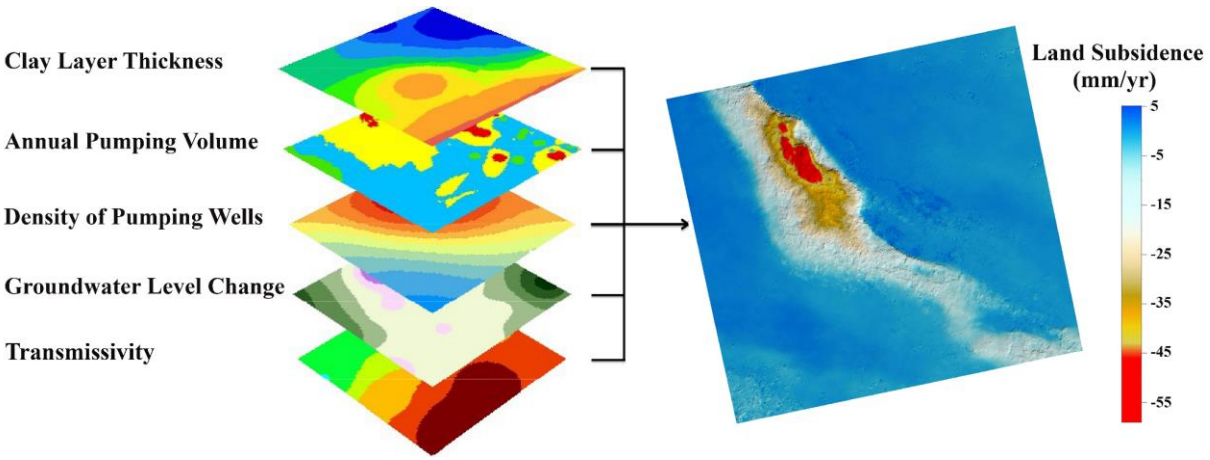

Figure 4. Schematic representation of the datasets used in the statistical methods to explore the controls on the subsidence rates and extent to the potential predictor variables (e.g., clay layer thickness, density of pumping wells, annual pumping volume, GWL change, and transmissivity (see Fig. S4)).

3.2.4 Elastic vs. inelastic aquifer response

Determining whether land subsidence is irrecoverable (inelastic) or recoverable (elastic) is important for water resources management strategies. Chaussard and Farr (2019) proposed a new method to isolate elastic from inelastic behavior with an Independent Component Analysis (ICA), which is a statistical and computational technique for separation of independent sources linearly mixed in a signal (Gualandi et al., 2017). We used the fixed-point algorithm, FastICA (Hyvärinen and Oja, 1997) and constrain the number of independent components (ICs) and their order of importance with a Principal Component Analysis (PCA) and the truncation of variance rule (Cattell, 1966; Chaussard et al., 2017). We apply the ICA to the Sentinel-1 data which has 1,408,439 samples (pixels) per epoch and 129 and 118 epochs (acquisitions between 2014 and 2020) for the ascending and descending orbits, respectively. Following a PCA, only one component was retained, explaining ~ 99.5% of the eigenvalues (compared to 99.6% with two components). For each IC we show (1) an eigenvalue time series, representing the magnitude of the component at each epoch and (2) a score map scaled by the contribution of retained components to the original data, highlighting the pixels with the observed eigenvalue time series.

306 **4 Results and analysis**

307 4.1 Spatial pattern of subsidence

308 Figure 5 shows the mean vertical and horizontal velocity maps in the YAP, decomposed
309 by the mean LOS velocity from ascending and descending orbits. The most significant
310 subsidence feature is an elongated northwest-southeast zone, south of Meybod and north of
311 Ashkezar (dark circles in Figs. 5a and b). This zone of subsidence, referred to as the Main
312 Subsidence Feature (MSF), covers an area of 234.45 km^2 (Fig. 5) and is seen in both Envisat
313 and Sentinel-1 datasets. While the overall shape and boundary of the MSF are consistent over the
314 17 years of InSAR data, the displacement rates and spatial extent appear to have changed over
315 time. The MSF extent has grown westward and toward the Yazd and Meybod cities in the
316 Sentinel data, with a subsidence rate of ~ 2 cm/yr in areas that appeared stable in the Envisat data
317 (indicated with the arrows in Fig. 5b). A differential vertical velocity map between the Envisat
318 and Sentinel data (Fig. 6a) confirms that the subsidence has expanded laterally along the
319 southern and western boundaries of the MSF. In Figure 6a, both an increase and a decrease in the
320 trend of subsidence by 2 cm/yr and 0.8 cm/yr are seen in the northeast and southwest parts of the
321 MSF, respectively, while a new subsidence area is detected southeast of Yazd city (red polygon
322 in Fig. 5b). Figure 6b shows a good agreement between the Envisat and Sentinel vertical motions
323 (with a correlation of 0.95 and a standard deviation of 0.7 cm/yr), while Figures 6c and 7c-d
324 show that Sentinel-1 and Envisat horizontal motions differ significantly, likely due to the greater
325 uncertainties of the Envisat data (Fig. 3). The 2014-2020 Sentinel-1 data reveals eastward ground
326 motion of 1.5 cm/yr on the western side of the MSF and westward motion at 1.2 cm/yr on the
327 eastern side of the MSF (Fig. 5d). Although Figure S4b shows that the distribution of pumping
328 wells is low between these areas with opposite horizontal motions, the volume of water extracted
329 appears to be sufficient to create this inner zone of contraction (Helm, 1994).
330

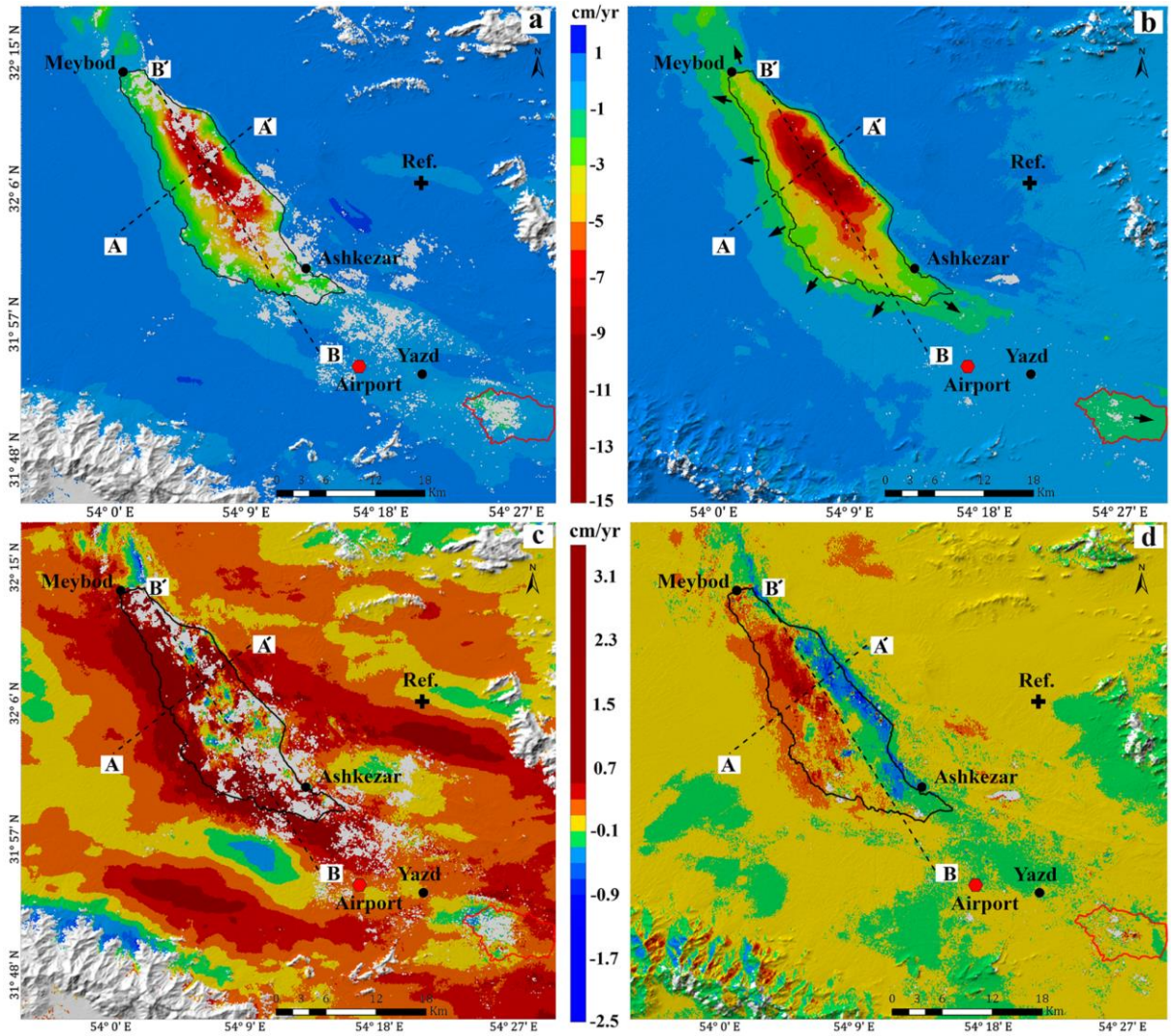

Figure 5. Annual mean deformation rate maps of the vertical component from (a) Envisat and (b) Sentinel-1 data, and the horizontal component from (c) Envisat and (d) Sentinel-1 data. Red colors show downward and eastward movements in the vertical and horizontal maps, respectively. Blue colors show westward movement in the horizontal component and areas of little or no deformation in the vertical maps. The black and red circles indicate cities and the Yazd Sadooghi International Airport (YSIA), respectively. The dashed lines show the locations of the two profiles ($A-A'$) and ($B-B'$) in Fig. 7. The cross indicates the reference pixel located in a stable area. The black and red polygons on (a) and (b) indicate the Main Subsidence Feature (MSF) and a new subsidence area to the southeast of Yazd city, respectively. The arrows in (b) indicate the direction of growth of the two subsiding areas.

331

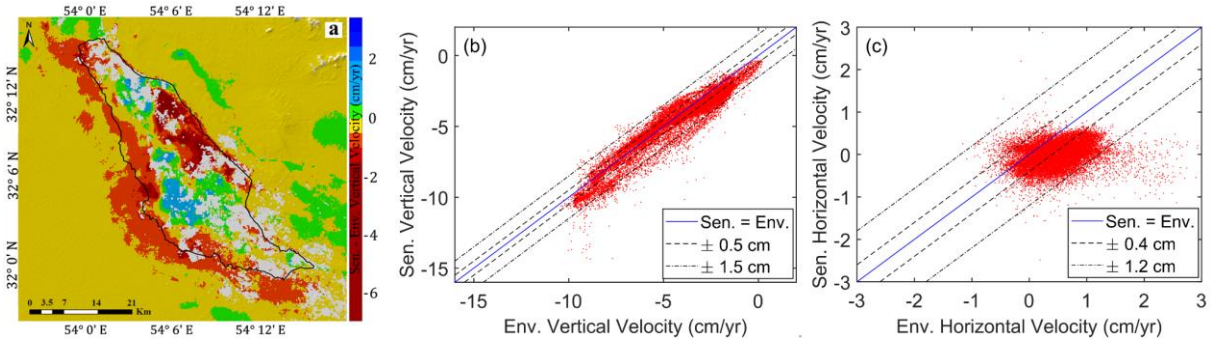

Figure 6. (a) Differential vertical velocity map between the Envisat and Sentinel data (Fig 5a and 5b). The black polygon shows the boundary of the MSF. Comparison between Envisat and Sentinel-1 (b) vertical velocities and (c) horizontal velocities over the MSF. The differential vertical rates fall within a three-sigma range of ± 1.5 cm/yr (dash-dotted lines), while the Sentinel-1 and Envisat horizontal motions do not appear correlated.

The profiles in Figure 7a-b confirm that the Envisat and Sentinel-1 data detect similar vertical deformation rates and extents. Significant differences include greater 2014-2020 (Sentinel-1) subsidence rates (1) on profile A-A' between 5 and 10 km (Fig. 7a, shaded area), and (2) on profile B-B' between 0 and 7 km (Fig. 7b, shaded area), highlighting the expansion of the subsiding area towards the south. In addition, both profiles show that in the center of the MSF subsidence rates accelerated by about 5 cm/yr between the Envisat and Sentinel-1 data. A localized area with almost 14 cm/yr of subsidence is observed for thirty pixels of the Sentinel-1 data (peak in Fig. 7b) and may represent a sinkhole or a collapsing structure, but optical data did not allow us to confirm this interpretation. Figure 7c confirms the existence of eastward motion on the west side of the MSF and a westward motion on the east side in the Sentinel-1 data. Figure 7d shows no clear east-west deformation in the N-S oriented profile and further illustrates the greater noise content of the Envisat data. The uncertainties of both vertical and horizontal rates along the profiles are shown in the inset plots, with Sentinel-1 data having a standard deviation of about 1 mm/yr along both profiles, and Envisat of 2 to 4 mm/yr (see Fig. S5 for maps of uncertainties). Over the entire study area, uncertainties are mostly < 2 mm/yr with means of 0.6 and 0.4 mm/yr for the Envisat and Sentinel-1 vertical components, and 0.4 and 0.3 mm/yr for the Envisat and Sentinel-1 horizontal components, respectively (Fig S5). Similarly, the uncertainties for both individual ascending and descending epochs of the Envisat and Sentinel-1 data are mostly < 2 mm (Fig. S6).

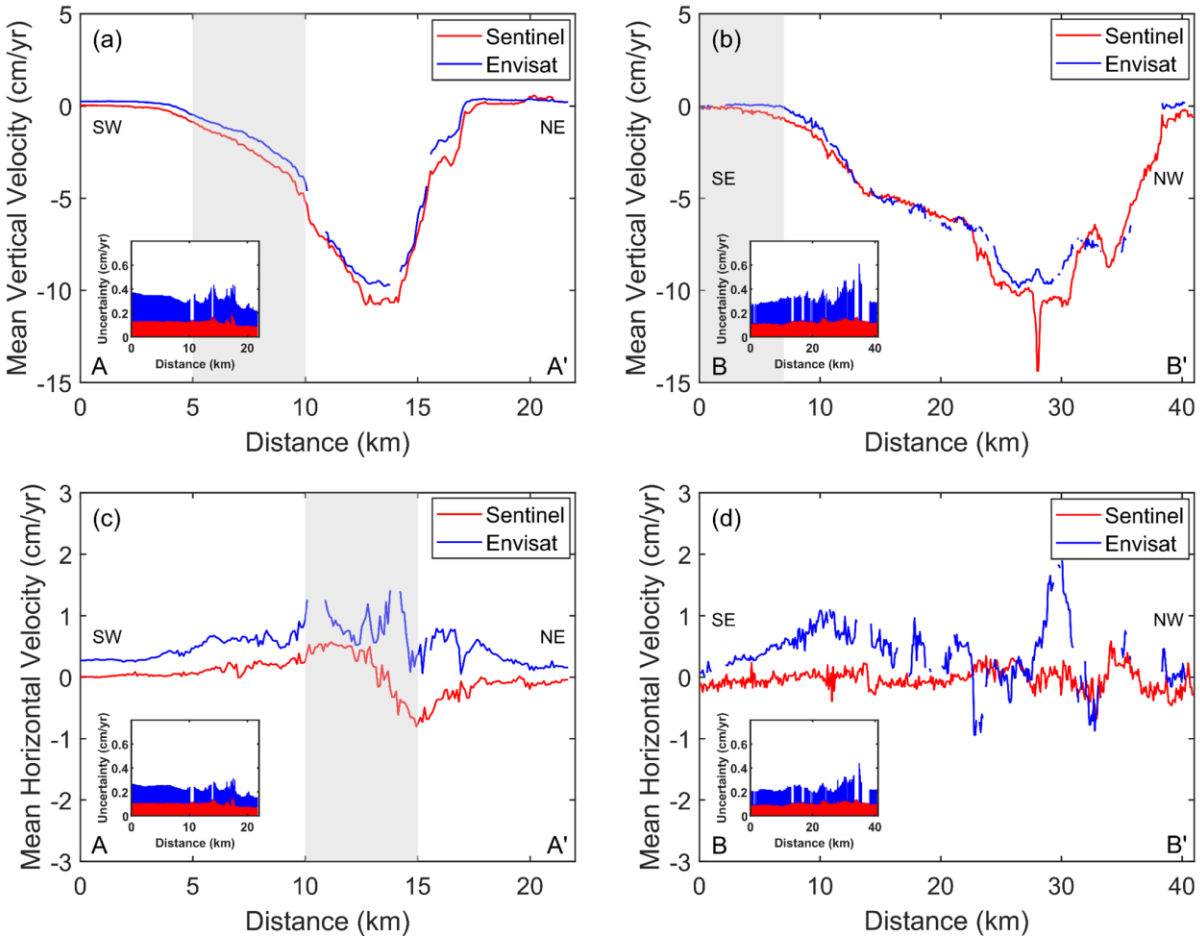

Figure 7. Mean vertical (a, b) and horizontal (c, d) velocities derived from Envisat (blue) and Sentinel-1 (red) data along the profiles ($A-A'$) and ($B-B'$) (locations shown in Fig. 5). The insets show the corresponding three-sigma uncertainties. The shaded areas highlight significantly different signals in the 2003-2010 Envisat and 2014-2020 Sentinel-1 data mentioned in the text.

353

354 4.2 Infrastructure monitoring

355 Comparison of our data with optical imagery reveal that land subsidence at varying rates
356 occurs in agricultural lands, urban areas, and industrial areas, potentially affecting factories and
357 infrastructures, such as roads and power grids. Table S4 provides a list of the infrastructures
358 located in subsiding areas. One of the most important infrastructures in the YAP is the Bandar
359 Abbas-Yazd-Ardakan Transit road. Figure 8b-e highlights the mean vertical and horizontal
360 velocities along different sections of the road as seen in the Sentinel-1 data. Section (**A**)
361 experiences rapid subsidence over a 40 km section with a peak subsidence rate of 14 cm/yr,
362 without significant horizontal motion. 1.5 km south-southwest of this section and 2 km northeast

of nearest residential areas (red circle in Fig. 8a), differential subsidence led to multiple ground fissures (Fig. 9). Section (**B**) experiences vertical displacement along a 25 km long section with a peak value of 13 cm/yr and no significant horizontal deformation. Section (**C**) experiences subsidence in the northernmost 10 km with a peak of 1.7 cm/yr and no significant horizontal motion.

Another important transportation structure is the 85-km-long Tehran-Bandar Abbas railway connecting the Yazd province to the Provinces of Isfahan and Kerman. This section, known as the Santo section, is one of the most trafficked rail lines of Iran. Figure 8e reveals two ~20 km-long subsiding sections with rates of 1.7 and 1.4 cm/yr, respectively, and no significant horizontal deformation. Subsidence of up to 2 cm/yr is also observed near the Yazd Sadooghi International Airport (YSIA) (see location in Fig. 5), which served 431,500 passengers in 2012, making it the 11th airport in Iran (Iranian Students' News Agency, 2013).

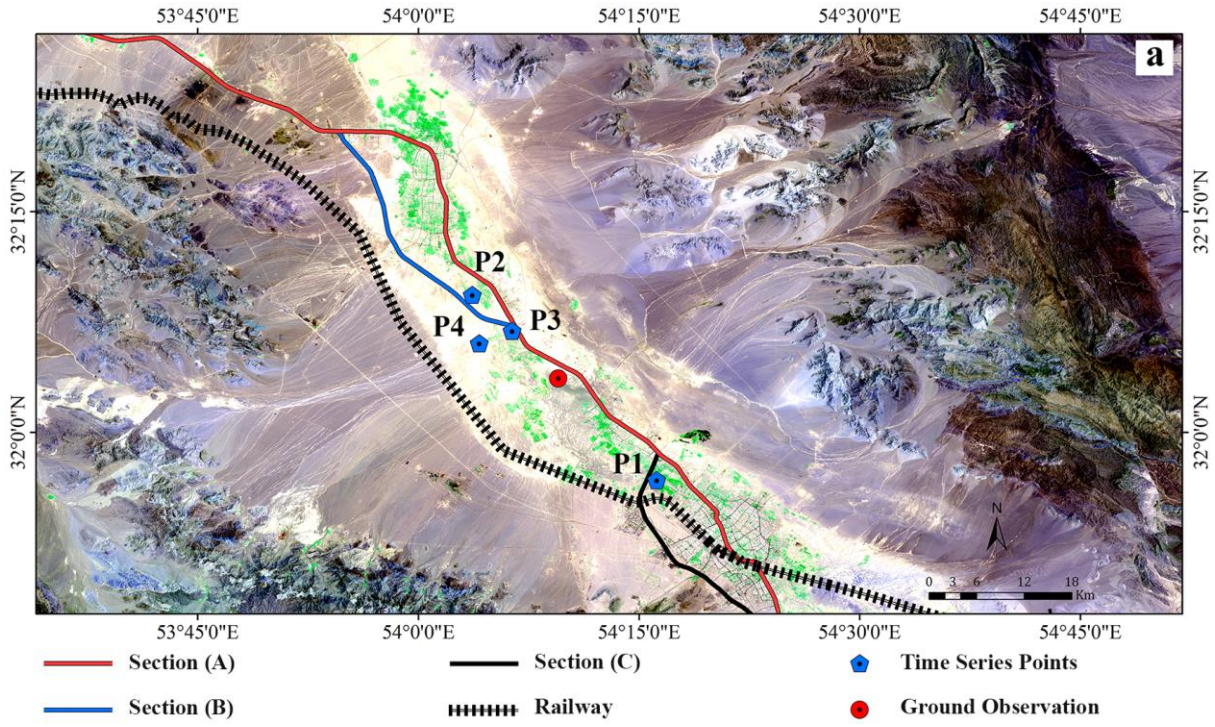

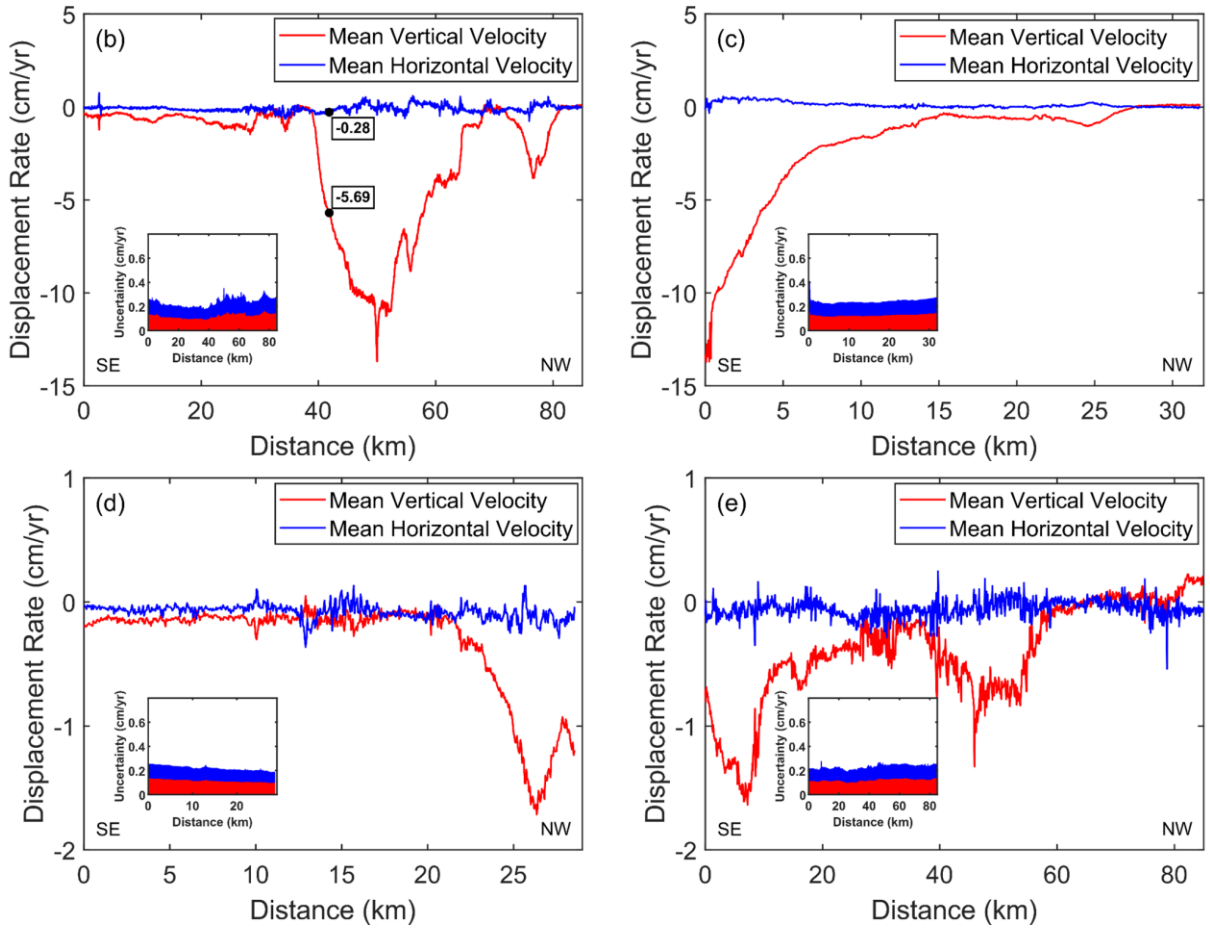

Figure 8. (a) Locations of the Bandar Abbas-Yazd-Ardakan Transit road sections (shown by the red, blue, and black lines), and of the railway (dashed black line). Blue and red symbols indicate the locations of time series (Fig. S7) and ground observation sites (Fig. 9), respectively. Mean Sentinel-1 vertical (red) and horizontal (blue) velocities for (b) Section (**A**), (c) Section (**B**), (d) Section (**C**) of the Badar Abbas-Yazd-Ardakan transit road, and (e) the Tehran-Bandar Abbas railway. The insets show the corresponding uncertainties. Black points in (a) indicate the mean Sentinel-1 vertical and horizontal velocities for the projected location of ground observation site on Section (**A**).

376

Figure 9. Photograph looking South taken from the location of the red circle on Figure 8a illustrating the fissures that have developed as a result of the observed differential subsidence (the person shows the scale).

5 Discussion

5.1 Potential causes of land subsidence

To gain further insights into the controls that hydrogeological and geological parameters may have on the rate and extent of the land subsidence, we carry out the following analysis.

5.1.1 Hydrogeological conditions

Figure S9a-b shows that between 2004 and 2019, a 3.2℃ increase (0.2 ℃/yr) in the average LST occurred in the region. Figure S9b shows that the LST was consistently higher throughout 2019 compared to 2004 (with the exception of January). Figure S9c shows that precipitation in 2018 amounted to approximatively only half of the 2003 precipitation (Sharafi and Karim, 2020), and while annual precipitation is highly variable, there is an overall trend towards decreasing rainfall in recent decades. These climatic changes (increased temperature and decreased precipitation) have likely led to an increased degree of dryness (Fig. S10b), which in turn influences natural recharge and discharge from evapotranspiration.

In addition, the Statistics Center of Iran reported a significant population growth of 3.67% per year between 1956 and 2016 (Fanni, 2006) in the cities located in the YAP (Fig. 1b and S2), leading to increased agricultural and industrial activities (e.g., tile and steel) (see Figs. 1c), which influences groundwater usage (Fig. S1). GWL fluctuations in the aquifer over 44 years (1974-2018) (Fig. 10) reveal an average 18 m drop in the YAP aquifer (Fig. 10a). Figure

10b shows that 4,010 million cubic meters were extracted from the aquifer during this period with 90%, 6.2%, and 3.8% used by the agriculture, urban, and industry sectors, respectively (Fig. S1b-e) (Iran's WRM Co., 2014).

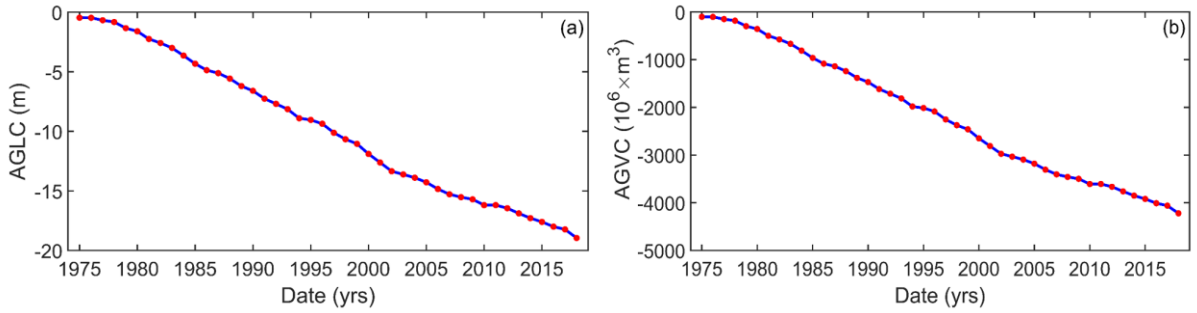

Figure 10. (a) Average annual accumulated groundwater level changes (AGLC) in meters (mean lowering of groundwater level of aquifer) and (b) total annual accumulated groundwater volume changes (AGVC) in million cubic meters, for the YAP aquifer system between 1974 and 2018 (Iran's WRM Co., 2014).

To assess the potential relationship between the GWL changes and observed deformation, the time series of converted-vertical displacement (see section 4.2) and GWL changes were determined at sites P1-P4 (locations shown in Fig. 8a). The converted-vertical displacement time series from the ascending data do not differ significantly from vertical time series converted from the descending data (Fig. S7). We use the ascending, converted-vertical displacement time series, which has 11 more acquisitions than the descending data, to compare to the GWL fluctuations in the probability and time domains (see method in section 4.2, Fig. S8).

Correlation values of 0.67 and 0.81 are observed between the converted-vertical displacements and the GWL changes at P1 and P4, respectively (Fig. S7), suggesting that GWL changes may influence the subsidence rates. At P2, although the time series of GWL changes and converted-vertical displacements have a correlation of 0.7, their trends differ significantly more than those observed at P1 and P4. Finally, at P3, the correlation between the converted-vertical displacements and the GWL changes is only of 0.21 (Fig. S7), suggesting that other factors also influence the subsidence rates.

Figure 11 shows the exceedance probability (EP) analysis of converted-vertical displacements and GWL changes. The duration curves of converted-vertical displacements (DDC) and GWL changes (GDC) mirror each other at P1 and P4, confirming that, at those

418 locations, the GWL changes and subsidence rates are related. In contrast, at P2, the slopes S_{DC} of
419 the GDC and DDC do not track one another, suggesting that other factors affect the subsidence
420 rates. At P3, for EP < 0.2, the S_{DC} of the GWL changes is greater than that of the converted-
421 vertical displacements, while for EP > 0.2, the S_{DC} for the GDC is smaller. These observations
422 suggest that the subsidence rates at P2 and P3 cannot be predicted solely from the observed
423 GWL changes. P2 and P3 are located in the area with the thickest clay deposits (Fig. S4a), which
424 may also influence the subsidence rates.
425

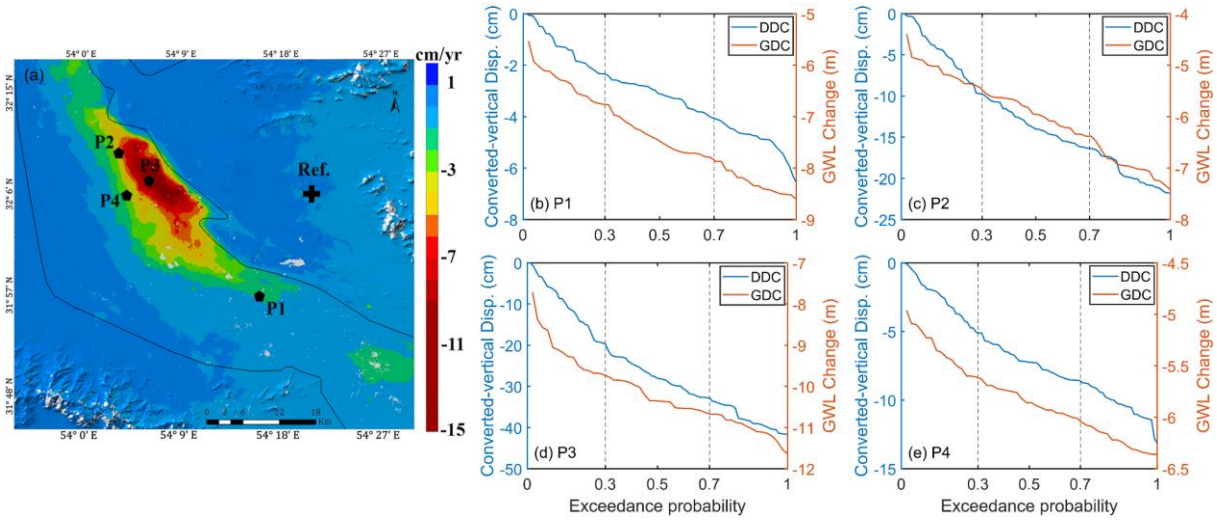

Figure 11. (a) Mean 2014-2020 Sentinel-1 vertical velocity map. The cross and black circles indicate the reference pixel and the P1-P4 site locations, respectively. (b-e) Duration curves of GWL changes (GDC, red) and converted-vertical displacements (DDC, blue) for P1 to P4 (b to e, respectively).

426

427 5.1.2 Geological settings

428 We explored the potential influence of the shallow clay layer thickness on the subsidence
429 rates and extent. The clays thickness increases towards the center of basin, reaching 134 meters
430 (Fig. S4a). We separate the clay thickness (C) observed throughout the YAP into five classes (C
431 ≤ 20 m, 20 m < C ≤ 40 m, 40 m < C ≤ 60 m, 60 m < C ≤ 80 m, and C > 80 m (Table 1)) and
432 compare the observed maximum and mean vertical velocities observed in areas of the valley
433 corresponding to each class (Table 1). The maximum vertical velocities (>10 cm/yr) observed in
434 the Envisat and Sentinel-1 data are located in areas with clay thicknesses >80 m. In contrast,
435 areas with clay thicknesses less than 20m show subsidence rates lower than 6 cm/yr. These

436 observations suggest that the clay thickness is an important factor influencing the subsidence
437 rates and extent.

Table 1. Maximum and mean vertical velocities observed in areas with various clay thicknesses.

Clay Layer Thickness (C) (m)	Dataset	Statistical Parameters (cm/yr)		
		Max	Mean	Std
C ≤ 20	Envisat	5.1	0.7	0.6
	Sentinel	5.7	0.9	0.7
20 < C ≤ 40	Envisat	5.6	0.6	0.9
	Sentinel	5.6	0.8	1.1
40 < C ≤ 60	Envisat	6.2	1.0	1.2
	Sentinel	6.1	1.3	1.4
60 < C ≤ 80	Envisat	7.2	0.8	1.2
	Sentinel	6.4	1.1	1.4
C > 80	Envisat	10.8	4.4	2.8
	Sentinel	14.6	4.9	2.8

438

439 5.2 Relative control on the rates and extent of observed land subsidence

440 To quantify the relative importance of hydrological and geological parameters previously
441 described (i.e., the clay layer thickness, annual pumping volume, GWL changes, density of
442 pumping wells, and transmissivity) on the observed land subsidence rates and extent, we used
443 MLR and SVR approaches (linear and non-linear regression methods, see method section 4.3;
444 Figure 12, and Table 2). Due to the low spatial resolution of climate parameters (LST and
445 precipitation), we do not use those variables in the MLR and SVR approaches. To estimate the
446 goodness of fit and compare the results with each other, we use the Relative RMSE (RRMSE
447 $= \frac{RMSE}{average\ (mean\ vertical\ velocity)}$) and r-squared ($R^2$) values.

448 Figure 12 shows that the single-variable MLR and SVR approaches, with the clay layer
449 thickness as a potential predictor, have the highest R^2 and lowest RRMSE of all single-variable
450 analyses, suggesting that the clay layer thickness has the strongest influence on the land
451 subsidence rates (RRMSEs of 0.95 to 1.32 and R^2 of 0.42 to 0.67). Among the bivariate
452 analyses, incorporating the clay layer thickness and the density of pumping wells improves the
453 R^2 by 26% and 34% for the Envisat data (MLR and SVR, respectively) and 15% and 25% for

454 the Sentinel-1 data (MLR and SVR, respectively); and decrease the RRMSE by 10% and 30%
455 for the Envisat data and 8% and 29% for the Sentinel-1 data (Table 2). These results suggest that
456 the density of pumping wells is the second most influential parameter after the clay thickness.
457 Figure 12 further confirms that the multi-variable analyses in which the clay layer thickness is
458 considered as a potential predictor variable perform best.
459

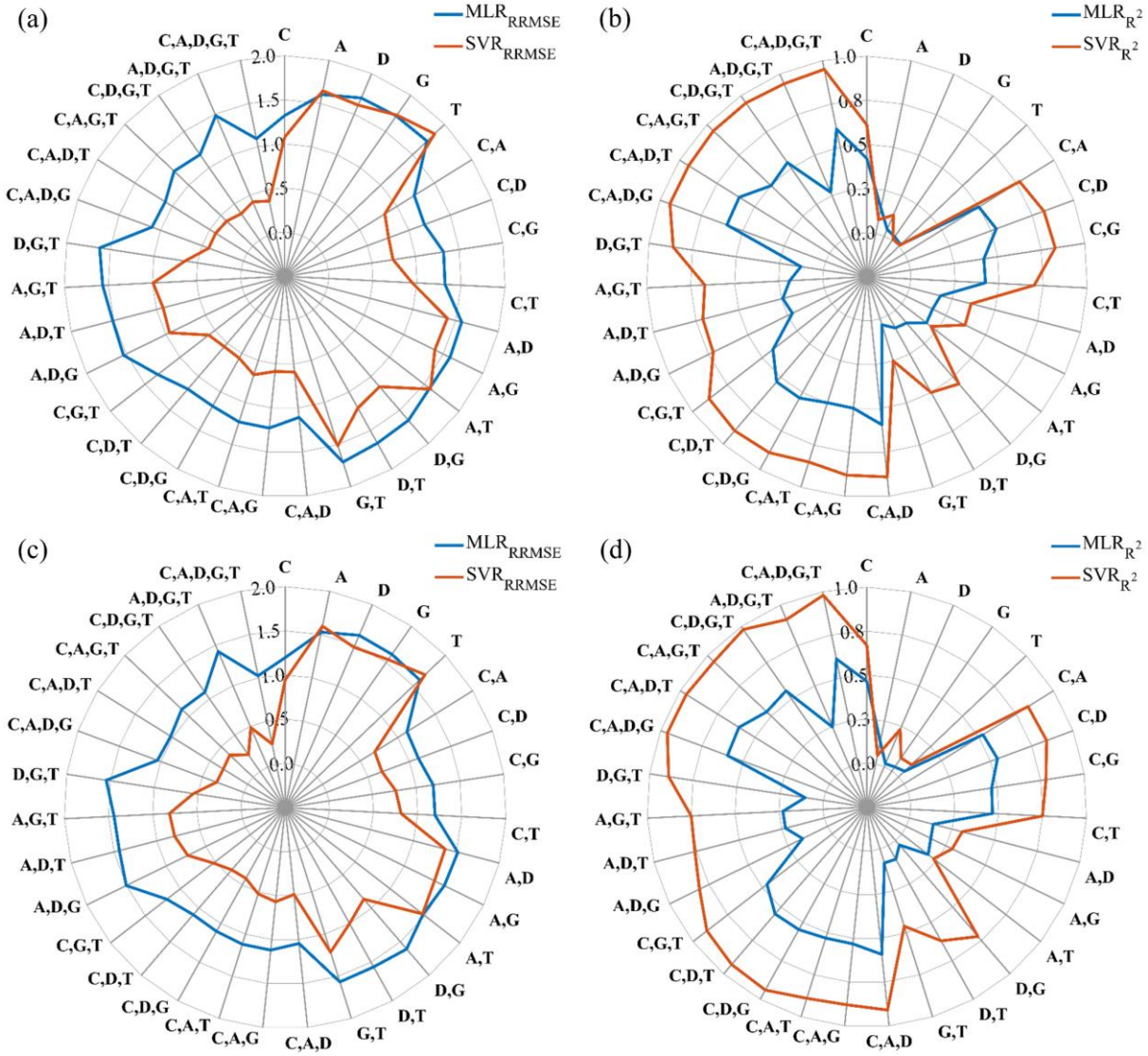

Figure 12. Spider plots illustrating the values of Relative RMSE (RRMSE) (a and c) and r-squared (R^2) (b and d) for all single- and multi-variable MLR and SVR analyses using several potential predictor variables (i.e., C: Clay Layer Thickness (m), A: Annual Pumping Volume (m^3/yr), D: Density of Pumping Well (Number/km^2), G: Groundwater Level (GWL) Change (m/yr), T: Transmissivity (m^2/day)) and the observed land subsidence from the Envisat (a,b) and Sentinel-1 datasets (c,d).

In addition, Table 2 shows that the SVR method performs better than the MLR method, decreasing the RRMSE between the predicted and observed subsidence by 66% for the Envisat and 77% for the Sentinel-1 datasets and increasing the R^2 by 58% for the Envisat and 61% for the Sentinel-1 datasets over the MLR approach. The better performance of the SVR is likely due to its nonlinearity, which is more accurate but also difficult to interpret (MathWorks, 2020). Including all potential predictor parameters, instead of only the clay layer thickness, decreases the value of RRMSE by 66% for the Envisat and 76% for the Sentinel-1 datasets in the SVR; and 17% for the Envisat and 15% for the Sentinel-1 datasets in the SVR. These results suggest that within the YAP, all parameters likely influence in various proportions the subsidence rates and extent, with the clay thickness being the dominant control.

Table 2. Results of a Multi-linear regression (MLR) approach and a support vector machine regression (SVR) approach considering the mean vertical velocity (MVV) as a response variable and the other variables as potential predictor variables (Fig. S4). The r-squared (R^2) and Relative RMSE are used to estimate the goodness of fit. In the SVR, the kernel functions (i.e., Gaussian or Radial Basis Function (RBF), Linear, Quadratic, and Cubic) determine the applied nonlinear transformation to the data before the SVM is trained (MathWorks, 2020).

Variables	Regression Type	Dataset	Model Type * / Kernel Function	R^2	RRMSE
C	MLR	Envisat	MVV = – 0.026 × C + 0.054	0.42	1.32
	SVR		Fine Gaussian	0.61	1.08
	MLR	Sentinel-1	MVV = – 0.039 × C – 0.015	0.47	1.20
	SVR		Fine Gaussian	0.67	0.95
C D	MLR	Envisat	MVV = – 0.028 × C – 0.820 × D + 0.547	0.53	1.18
	SVR		Fine Gaussian	0.82	0.75

	MLR	Sentinel-1	MVV = – 0.042 × C – 1.032 × D + 0.649	0.54	1.11
	SVR		Fine Gaussian	0.84	0.67
C D A G K	MLR	Envisat	MVV = – 0.025 × C – 0.860 × D – 1.612E-6 × A + 0.191 × G + 0.0002 × T + 0.693	0.60	1.09
	SVR		Fine Gaussian	0.95	0.37
	MLR	Sentinel-1	MVV = – 0.039 × C – 1.143 × D – 2.076E-6 × A + 0.489 × G + 0.0004 × T + 0.887	0.61	1.02
	SVR		Fine Gaussian	0.98	0.23

[*] MVV: Mean Vertical Velocity (cm/yr), C: Clay Layer Thickness (m), A: Annual Pumping Volume (m^3/yr), D: Density of Pumping Well ($Number/km^2$), G: Groundwater Level (GWL) Change (m/yr), T: Transmissivity (m^2/day).

We performed a sensitivity analysis to quantify the relative importance of each potential predictor variables to the predicted land subsidence using the MLR method (Li and Merchant, 2013; Parizi et al., 2019) as follow:

$$PV(j) = \frac{AV_{rw}(j) - AV_{rw}}{AV_{rw}} \times 100$$

where PV is the percentage of variation in the predicted subsidence; $AV_{rw}(j)$ is the predicted annual subsidence (with j representing each potential predictor variable), and AV_{rw} is the predicted annual land subsidence considering all potential predictor variables. Figure 13 shows that the clay thickness is the dominant parameter in explaining the variability of land subsidence rates. The pumping well density is the second most influential parameter, and other parameters have a significantly lower relative importance. In other words, for a similar distribution of pumping wells and annual pumping volume, thicker clays experience greater compaction.

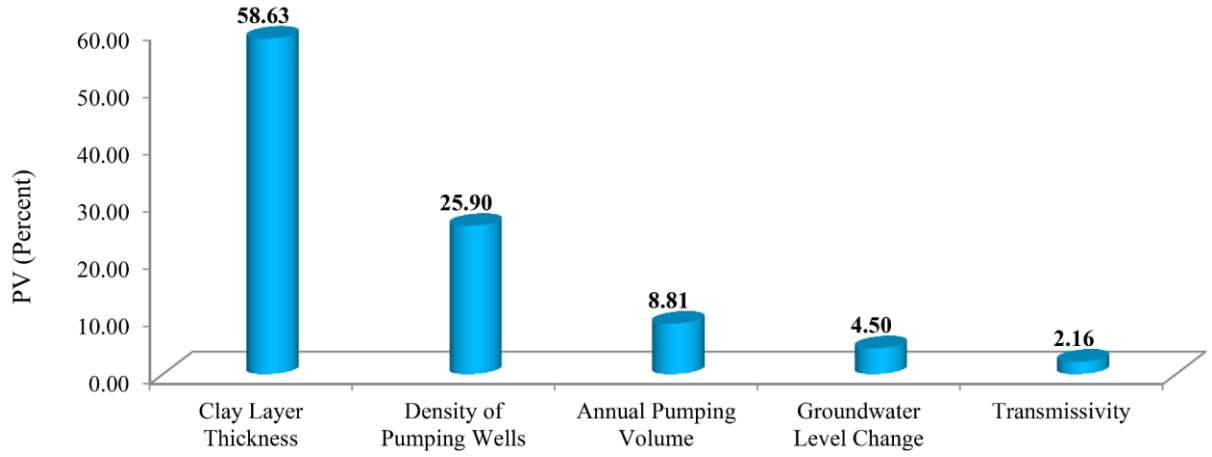

Figure 13. Percentage of variation (PV) of land subsidence explained by each of the potential predictor variables used in the MLR method.

485

486 5.3 Elastic vs. inelastic behavior

487 When an aquifer system experiences greater groundwater-level lowering than previously
488 experienced (i.e. the stress exceeds the pre-consolidation stress), pore spaces collapse
489 permanently, resulting in inelastic deformation (Carlson et al., 2020), which may manifest itself
490 in the formation of surface fissures and cracks in areas of large differential compaction. Because
491 the inelastic compressibility of aquitards is one to three orders of magnitude larger than the
492 elastic compressibility of aquitards and aquifers (Pavelko, 2004; Riley, 1998), most inelastic
493 deformation occurs in aquitard layers (Chaussard et al., 2014a; Chaussard et al., 2017). To
494 evaluate the proportion of elastic to inelastic surface deformation, we applied the ICA approach
495 of Chaussard and Farr (2019) to the Sentinel-1 converted-vertical deformation time series (Fig.
496 14). The eigenvalue of one component (IC1) corresponds to 99.5% of the sum of all the non-zero
497 eigenvalues, while a second component (IC2) retains only 0.1% of the eigenvalues. The spatial
498 extent of the IC1 positive score values is comparable to the mean vertical Sentinel-1 velocity
499 map (Fig. 5b), while the IC1 eigenvector time series highlights a nearly linear trend between
500 2014 and 2020 with a slope of -2.1 (in eigenvector/year units) (-15.7 in cm/yr units) (Fig. 14a).
501 While IC1 is the only statistically significant component, we show the results of IC2 for
502 reference. The IC2 score map shows negative values in the north and south and positive values in
503 the west (Fig. 14c), and an eigenvector time series with a slight downward trend and a slope of -
504 0.3 (in eigenvector/year units) (-0.001 in cm/yr unit) (Fig. 14a). The long-wavelength spatial
505 signal observed in the IC2 score map, combined with the low slope observed in the eigenvector

time series suggest that IC2 likely captures noise associated with orbital errors that were not entirely accounted for in the processing. As no clear seasonality or short term deformation is observed, the ICA suggests that all the deformation observed in the YAP is inelastic and captured by IC1. This is in agreement with observations made in the Mexico City Valley (Chaussard et al., 2021) and contrasts with observations made in the Central Valley and the Santa Clara Valley aquifers, California, USA where multiple short-term elastic deformation signals were isolated (Chaussard and Farr, 2019; Chaussard et al., 2017; Chaussard et al., 2014b).

Figure 14d suggests a positive correlation between the spatial extent of positive IC1 score values (subsidence) and the clay layer thickness, while Figure 14e suggests a positive correlation between the extent of the northern area with positive score values in IC1 (subsidence) and the area with maximum GWL decline (blue in Fig. 14e). Figure 14d also reveals that GWL declines $\geq$ 0.5 m/yr exist in the entirety of the area experiencing subsidence (positive score values in IC1). These observations suggest that the amplitude of the land subsidence is controlled by the thickness of the clay layer once a threshold of GWL decline is reached. These results confirm that (1) the deformation in the YAP is irreversible in locations where a minimum GWL is reached, leading to stress exceeding the pre-consolidation stress (which accounts for 85% of spatial extent of the subsiding area), and (2) in those locations the subsidence rates are constant and mostly controlled by the clays-layer thickness. As clay compaction lags behind the groundwater levels lowering (due to clays' low hydraulic conductivity), the continuous linear subsidence suggests that the clay compaction has not yet "caught-up" with the current and continuously evolving stress in the aquifer system, as observed in Mexico City (Chaussard et al., 2021). The aquitard is draining naturally at constant rates, resulting in the observed mostly constant subsidence rates that can be predicted from the aquitard thickness.

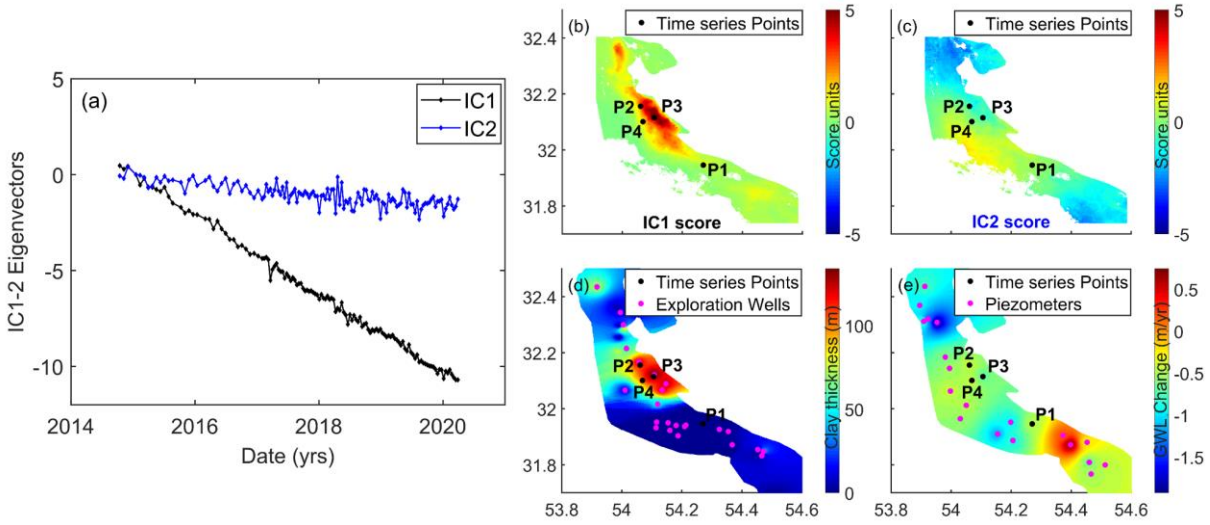

Figure 14. (a) Eigenvector time series analysis of IC1 (black) and IC2 (blue) derived from the converted-vertical-ascending Sentinel-1 data (see Fig. S11 for corresponding results for the converted-vertical-descending orbit Sentinel-1 data). (b, c) Score maps of (b) IC1 and (c) IC2. Black dots show the locations of the points with time series shown in Figure S7. (d) Map of the clay thickness interpolated between exploration wells (pink dots). (e) 2014-2020 mean GWL change map interpolated between piezometers (pink dots).

6 Conclusions

An InSAR time series analysis of Envisat and Sentinel-1 data in the YAP from 2003 to 2020 reveals land subsidence at rates up to 15 cm/yr within an elongated northwest-southeast zone of approximately 234.45 km^2. While the overall shape of the subsiding area did not change over the past 17 years, it grew laterally. Our data also reveals eastward motion at ~1.5 cm/yr and westward motion at ~1.2 cm/yr on the western and eastern sides of the subsiding area, respectively, as a result of the radial strain changes across the subsiding zone. Over 25 km of the Bandar Abbas-Yazd-Ardakan Transit road is affected by subsidence rates up to 5 cm/yr and the nearby airport (YSIA) is subsiding at ~2 cm/yr. While the YAP experienced a significant lowering in the groundwater levels in the past decades, regression analyses and duration curves of GWL changes and displacements at sites P2 and P3 show that the thickness of a shallow clay layer has the greatest correlation with the observed subsidence rates. Finally, an Independent Component Analysis (ICA) reveals that all the subsidence observed in the YAP is inelastic and thus irreversible and is caused by clay compaction. The clay layer aquitard is draining at constant rates, resulting in the observed, effectively linear subsidence rates. These results highlight the

547 need to develop and enforce sustainable water management strategies to protect the infrastructure
548 and groundwater resources in central Iran.

549 **Acknowledgments**

550 This work was supported by the National Natural Science Foundation of China (NSFC) Project
551 (Grant No. 12073012) and the CAS-TWAS President's Fellowship supporting the first author as
552 an International Ph.D. student. Chaussard is supported by a National Aeronautics and Space
553 Administration Grant Number 80NSSC19K0741.
554 The Envisat original data are copyrighted by the European Space Agency (ESA) and were
555 provided freely through the ESA archive (https://esar-ds.eo.esa.int/oads/access/). The Sentinel-1
556 dataset are made available by the ESA and distributed and archived through the Alaska Satellite
557 Facility (ASF) (https://www.asf.alaska.edu/sentinel/). Land Surface Temperature (LST) data was
558 obtained from the Google Earth Engine (GEE) Data Catalog
559 (https://developers.google.com/earth-engine/datasets). The ERA5 data and Shuttle Radar
560 Topography Mission (SRTM) Digital Elevation Model (DEM) data were provided through the
561 Copernicus Climate Data Store (https://cds.climate.copernicus.eu/#!/home) and the NASA's
562 Land Processes Distributed Active Archive Center (LP DAAC), located at the USGS Earth
563 Resources Observation and Science (EROS) Center (https://e4ftl01.cr.usgs.gov/MEASURES/),
564 respectively. The hydrological and geological data (i.e., groundwater level, logs of exploration
565 wells, pumping wells, and precipitation) were obtained from the Geological Survey and Mineral
566 Explorations of Iran (GSI) (https://gsi.ir/en) and Regional Water Company of Yazd
567 (https://www.yzrw.ir/?l=EN). The authors would like to thank the Geological Survey & Mineral
568 Explorations, Forests, Range, and Watershed Management Organization, Iran's Water Resources
569 Management Company, and Mr. Kamal Karimi Zarchi who helped us to visit the Yazd-Ardakan
570 Plain and collect the valuable ground observations of fissures and cracks for this study. The
571 Miami INsar Time-series software in PYthon (MintPy), InSAR Computing Environment (ISCE)
572 software, and Python 3 Atmospheric Phase Screen (PyAPS) are the open-source and available on
573 (https://github.com/insarlab/MintPy), (http://earthdef.caltech.edu/#), and
574 (https://github.com/isce-framework/isce2), respectively.
575

576 **References**

577 Abdollahi, S., Pourghasemi, H. R., Ghanbarian, G. A., and Safaeian, R.: Prioritization of effective factors in the
578 occurrence of land subsidence and its susceptibility mapping using an SVM model and their different kernel
579 functions, Bulletin of Engineering Geology and the Environment, 78, 4017-4034, 2019.
580 Abidin, H. Z., Djaja, R., Darmawan, D., Hadi, S., Akbar, A., Rajiyowiryono, H., Sudibyo, Y., Meilano, I., Kasuma,
581 M., and Kahar, J.: Land subsidence of Jakarta (Indonesia) and its geodetic monitoring system, Natural Hazards, 23,
582 365-387, 2001.
583 Amani, M., Salehi, B., Mahdavi, S., Masjedi, A., and Dehnavi, S.: Temperature-vegetation-soil moisture dryness
584 index (tvmdi), Remote sensing of environment, 197, 1-14, 2017.
585 Amelung, F., Galloway, D. L., Bell, J. W., Zebker, H. A., and Laczniak, R. J.: Sensing the ups and downs of Las
586 Vegas: InSAR reveals structural control of land subsidence and aquifer-system deformation, Geology, 27, 483-486,
587 1999.
588 Amighpey, M. and Arabi, S.: Studying land subsidence in Yazd province, Iran, by integration of InSAR and
589 levelling measurements, Remote Sensing Applications: Society and Environment, 4, 1-8, 2016.
590 Amin, A. and Bankher, K.: Causes of land subsidence in the Kingdom of Saudi Arabia, Natural Hazards, 16, 57-63,
591 1997.

592 Anderssohn, J., Wetzel, H.-U., Walter, T. R., Motagh, M., Djamour, Y., and Kaufmann, H.: Land subsidence pattern
593 controlled by old alpine basement faults in the Kashmar Valley, northeast Iran: results from InSAR and levelling,
594 Geophysical Journal International, 174, 287-294, 2008.
595 Avtar, R., Tripathi, S., Aggarwal, A. K., and Kumar, P.: Population–Urbanization–Energy Nexus: A Review,
596 Resources, 8, 136, 2019.
597 Babaee, S., Mousavi, Z., Masoumi, Z., Malekshah, A. H., Roostaei, M., and Aflaki, M.: Land subsidence from
598 interferometric SAR and groundwater patterns in the Qazvin plain, Iran, International Journal of Remote Sensing,
599 41, 4780-4798, 2020.
600 Baum, R. L., Galloway, D. L., and Harp, E. L.: Landslide and land subsidence hazards to pipelines, Geological
601 Survey (US)2331-1258, 2008.
602 Bell, J. W., Amelung, F., Ferretti, A., Bianchi, M., and Novali, F.: Permanent scatterer InSAR reveals seasonal and
603 long-term aquifer-system response to groundwater pumping and artificial recharge, Water Resources Research, 44,
604 2008.
605 Berardino, P., Fornaro, G., Lanari, R., and Sansosti, E.: A new algorithm for surface deformation monitoring based
606 on small baseline differential SAR interferograms, IEEE Transactions on geoscience and remote sensing, 40, 2375-
607 2383, 2002.
608 Bozzano, F., Esposito, C., Franchi, S., Mazzanti, P., Perissin, D., Rocca, A., and Romano, E.: Understanding the
609 subsidence process of a quaternary plain by combining geological and hydrogeological modelling with satellite
610 InSAR data: The Acque Albule Plain case study, Remote Sensing of Environment, 168, 219-238, 2015.
611 Bürgmann, R., Rosen, P. A., and Fielding, E. J.: Synthetic aperture radar interferometry to measure Earth's surface
612 topography and its deformation, Annual review of earth and planetary sciences, 28, 169-209, 2000.
613 Carlson, G., Shirzaei, M., Ojha, C., and Werth, S.: Subsidence-Derived Volumetric Strain Models for Mapping
614 Extensional Fissures and Constraining Rock Mechanical Properties in the San Joaquin Valley, California, Journal of
615 Geophysical Research: Solid Earth, 2020. e2020JB019980, 2020.
616 Castellarin, A., Galeati, G., Brandimarte, L., Montanari, A., and Brath, A.: Regional flow-duration curves: reliability
617 for ungauged basins, Advances in Water Resources, 27, 953-965, 2004.
618 Cattell, R. B.: The scree test for the number of factors, Multivariate behavioral research, 1, 245-276, 1966.
619 Chaussard, E., Amelung, F., Abidin, H., and Hong, S.-H.: Sinking cities in Indonesia: ALOS PALSAR detects rapid
620 subsidence due to groundwater and gas extraction, Remote sensing of environment, 128, 150-161, 2013.
621 Chaussard, E., Bürgmann, R., Shirzaei, M., Fielding, E. J., and Baker, B.: Predictability of hydraulic head changes
622 and characterization of aquifer-system and fault properties from InSAR-derived ground deformation, Journal of
623 Geophysical Research: Solid Earth, 119, 6572-6590, 2014a.
624 Chaussard, E. and Farr, T. G.: A new method for isolating elastic from inelastic deformation in aquifer systems:
625 application to the San Joaquin Valley, CA, Geophysical Research Letters, 46, 10800-10809, 2019.
626 Chaussard, E., Havazli, E., Fattahi, H., Cabral-Cano, E., and Solano-Rojas, D.: Over a Century of Sinking in Mexico
627 City: No Hope for Significant Elevation and Storage Capacity Recovery, Journal of Geophysical Research: Solid
628 Earth, n/a, e2020JB020648, 2021.
629 Chaussard, E., Milillo, P., Bürgmann, R., Perissin, D., Fielding, E. J., and Baker, B.: Remote sensing of ground
630 deformation for monitoring groundwater management practices: Application to the Santa Clara Valley during the
631 2012–2015 California drought, Journal of Geophysical Research: Solid Earth, 122, 8566-8582, 2017.
632 Chaussard, E., Wdowinski, S., Cabral-Cano, E., and Amelung, F.: Land subsidence in central Mexico detected by
633 ALOS InSAR time-series, Remote sensing of environment, 140, 94-106, 2014b.
634 Chen, C. and Zebker, A.: SNAPHU: statisticalcost, network-flow algorithm for phase unwrapping, Retrieved April,
635 27, 2016, 2003.
636 Chen, P.-H., Fan, R.-E., and Lin, C.-J.: A study on SMO-type decomposition methods for support vector machines,
637 IEEE Trans. Neural Networks, 17, 893-908, 2006.
638 Cheremisinoff, N. P.: Groundwater remediation and treatment technologies, Elsevier, 1998.
639 Conway, B. D.: Land subsidence and earth fissures in south-central and southern Arizona, USA, Hydrogeology
640 journal, 24, 649-655, 2016.
641 Emil, M. K., Sultan, M., Al-Akhras, K., Gebremichael, E., Izadi, M., and Karki, S.: Detecting and monitoring
642 ground deformation using InSAR time series in arid environments; Doha City and its surroundings, Qatar, AGUFM,
643 2018, G41B-0704, 2018.
644 Esfanjary, E.: Persian historic urban landscapes: interpreting and managing Maibud over 6000 years, Edinburgh
645 University Press, 2018.
646 ESRI: http://desktop.arcgis.com/en/arcmap/latest/tools/spatial-analyst-toolbox/an-overview-of-the-interpolation-
647 tools.htm, last access: 15 November 2019, 2012.

Fanni, Z.: Cities and urbanization in Iran after the Islamic revolution, Cities, 23, 407-411, 2006.

Galloway, D. L. and Burbey, T. J.: Regional land subsidence accompanying groundwater extraction, Hydrogeology Journal, 19, 1459-1486, 2011.

Galloway, D. L., Hudnut, K. W., Ingebritsen, S., Phillips, S. P., Peltzer, G., Rogez, F., and Rosen, P.: Detection of aquifer system compaction and land subsidence using interferometric synthetic aperture radar, Antelope Valley, Mojave Desert, California, Water Resources Research, 34, 2573-2585, 1998.

Geological Survey of Iran: https://gsi.ir/en, last access: 15 November 2019, 1997.

Ghotbi, S., Wang, D., Singh, A., Blöschl, G., and Sivapalan, M.: A New Framework for Exploring Process Controls of Flow Duration Curves, Water Resources Research, 56, e2019WR026083, 2020a.

Ghotbi, S., Wang, D., Singh, A., Mayo, T., and Sivapalan, M.: Climate and Landscape Controls of Regional Patterns of Flow Duration Curves Across the Continental United States: Statistical Approach, Water Resources Research, 56, e2020WR028041, 2020b.

Gido, N. A., Amin, H., Bagherbandi, M., and Nilfouroushan, F.: Satellite monitoring of mass changes and ground subsidence in Sudan's oil fields using GRACE and Sentinel-1 data, Remote Sensing, 12, 1792, 2020.

Gong, G., Mattevada, S., and O'bryant, S. E.: Comparison of the accuracy of kriging and IDW interpolations in estimating groundwater arsenic concentrations in Texas, Environmental research, 130, 59-69, 2014.

Gualandi, A., Avouac, J.-P., Galetzka, J., Genrich, J. F., Blewitt, G., Adhikari, L. B., Koirala, B. P., Gupta, R., Upreti, B. N., and Pratt-Sitaula, B.: Pre-and post-seismic deformation related to the 2015, Mw7. 8 Gorkha earthquake, Nepal, Tectonophysics, 714, 90-106, 2017.

Haghighi, M. H. and Motagh, M.: Ground surface response to continuous compaction of aquifer system in Tehran, Iran: Results from a long-term multi-sensor InSAR analysis, Remote sensing of environment, 221, 534-550, 2019.

Hanson, R., Anderson, S., and Pool, D.: Simulation of ground-water flow and potential land subsidence, Avra Valley, Arizona, US Department of the Interior, US Geological Survey, 1990.

Helm, D. C.: Horizontal aquifer movement in a Theis-Thiem confined system, Water Resources Research, 30, 953-964, 1994.

Hersbach, H., Bell, B., Berrisford, P., Hirahara, S., Horányi, A., Muñoz-Sabater, J., Nicolas, J., Peubey, C., Radu, R., and Schepers, D.: The ERA5 global reanalysis, Quarterly Journal of the Royal Meteorological Society, 146, 1999-2049, 2020.

Hoffmann, J., Zebker, H. A., Galloway, D. L., and Amelung, F.: Seasonal subsidence and rebound in Las Vegas Valley, Nevada, observed by synthetic aperture radar interferometry, Water Resources Research, 37, 1551-1566, 2001.

Hooper, A.: A multi-temporal InSAR method incorporating both persistent scatterer and small baseline approaches, Geophysical Research Letters, 35, 2008.

Hu, X., Lu, Z., and Wang, T.: Characterization of hydrogeological properties in salt lake valley, Utah, using InSAR, Journal of Geophysical Research: Earth Surface, 123, 1257-1271, 2018.

Hyvärinen, A. and Oja, E.: A fast fixed-point algorithm for independent component analysis, Neural computation, 9, 1483-1492, 1997.

Iran Meteorological Organization: http://www.irimo.ir/eng/index.php, last access: 15 November 2019, 2018.

Iran's WRM Co.: http://wrbs.wrm.ir/, last access: 15 November 2019, 2014.

Iranian Students' News Agency: https://www.isna.ir/news/91101207946/, last access: 08 December 2020, 2013.

Jarvis, A., Reuter, H., Nelson, A., and Guevara, E.: Hole-Filled Seamless SRTM Data V4: International Centre for Tropical Agriculture (CIAT): http, srtm. csi. cgiar. org, accessed, 31, 2008.

Jin, S. and Su, K.: PPP models and performances from single-to quad-frequency BDS observations, Satellite Navigation, 1, 1-13, 2020.

Jolivet, R., Agram, P. S., Lin, N. Y., Simons, M., Doin, M. P., Peltzer, G., and Li, Z.: Improving InSAR geodesy using global atmospheric models, Journal of Geophysical Research: Solid Earth, 119, 2324-2341, 2014.

Jolivet, R., Grandin, R., Lasserre, C., Doin, M. P., and Peltzer, G.: Systematic InSAR tropospheric phase delay corrections from global meteorological reanalysis data, Geophysical Research Letters, 38, 2011.

Julio-Miranda, P., Ortíz-Rodríguez, A., Palacio-Aponte, A., López-Doncel, R., and Barboza-Gudiño, R.: Damage assessment associated with land subsidence in the San Luis Potosi-Soledad de Graciano Sanchez metropolitan area, Mexico, elements for risk management, Natural Hazards, 64, 751-765, 2012.

Laity, J. J.: Deserts and desert environments, John Wiley & Sons, 2009.

Li, R. and Merchant, J. W.: Modeling vulnerability of groundwater to pollution under future scenarios of climate change and biofuels-related land use change: A case study in North Dakota, USA, Science of the total environment, 447, 32-45, 2013.

Marinkovic, P. and Larsen, Y.: Consequences of long-term ASAR local oscillator frequency decay—An empirical study of 10 years of data, 2013.
MathWorks: https://www.mathworks.com/help/stats/choose-regression-model-options.html, last access: 15 January 2021, 2020.
MathWorks: https://www.mathworks.com/help/stats/understanding-support-vector-machine-regression.html, last access: 15 January 2020, 2019.
Motagh, M., Shamshiri, R., Haghighi, M. H., Wetzel, H.-U., Akbari, B., Nahavandchi, H., Roessner, S., and Arabi, S.: Quantifying groundwater exploitation induced subsidence in the Rafsanjan plain, southeastern Iran, using InSAR time-series and in situ measurements, Engineering geology, 218, 134-151, 2017.
Motagh, M., Walter, T. R., Sharifi, M. A., Fielding, E., Schenk, A., Anderssohn, J., and Zschau, J.: Land subsidence in Iran caused by widespread water reservoir overexploitation, Geophysical Research Letters, 35, 2008.
Ojha, C., Shirzaei, M., Werth, S., Argus, D. F., and Farr, T. G.: Sustained groundwater loss in California's Central Valley exacerbated by intense drought periods, Water resources research, 54, 4449-4460, 2018.
Parizi, E., Hosseini, S. M., Ataie-Ashtiani, B., and Simmons, C. T.: Representative Pumping Wells Network to Estimate Groundwater Withdrawal From Aquifers: Lessons from a Developing Country, Iran, Journal of Hydrology, 2019. 124090, 2019.
Pavelko, M. T.: Estimates of hydraulic properties from a one-dimensional numerical model of vertical aquifer-system deformation, Lorenzi Site, Las Vegas, Nevada, US Department of the Interior, US Geological Survey, 2004.
Porter, J. R., Xie, L., Challinor, A. J., Cochrane, K., Howden, S. M., Iqbal, M. M., Lobell, D. B., Travasso, M. I., Field, C. B., and Barros, V. R.: Climate change 2014: impacts, adaptation, and vulnerability. Part A: global and sectoral aspects. Contribution of Working Group II to the Fifth Assessment Report of the Intergovernmental Panel on Climate Change, Food security and food production systems, 2014. 485-533, 2014.
Regional Water Company of Yazd: Yazd Water Data. Internal Reports, Regional Water Company of Yazd, 2014.
Riley, F. S.: Mechanics of aquifer systems—The scientific legacy of Joseph F. Poland, 1998, 13-27.
Sawicz, K., Wagener, T., Sivapalan, M., Troch, P. A., and Carrillo, G.: Catchment classification: empirical analysis of hydrologic similarity based on catchment function in the eastern USA, Hydrology and Earth System Sciences, 15, 2895-2911, 2011.
Schmidt, D. A. and Bürgmann, R.: Time-dependent land uplift and subsidence in the Santa Clara valley, California, from a large interferometric synthetic aperture radar data set, Journal of Geophysical Research: Solid Earth, 108, 2003.
Sharafi, S. and Karim, N. M.: Investigating trend changes of annual mean temperature and precipitation in Iran, Arabian Journal of Geosciences, 13, 1-11, 2020.
SHIBASAKI, T.: The hydrologic balance in the land subsidence phenomena, Land Subsidence, 1, 201-215, 1969.
Sterrett, R. J.: Groundwater and wells, Johnson Screens, 2007.
TAMAB: National Groundwater Resources Status, Basic Studies Office, Iran Water Resources Management Company, 2004.
Tien Bui, D., Shahabi, H., Shirzadi, A., Chapi, K., Pradhan, B., Chen, W., Khosravi, K., Panahi, M., Bin Ahmad, B., and Saro, L.: Land subsidence susceptibility mapping in south korea using machine learning algorithms, Sensors, 18, 2464, 2018.
Tizzani, P., Berardino, P., Casu, F., Euillades, P., Manzo, M., Ricciardi, G., Zeni, G., and Lanari, R.: Surface deformation of Long Valley caldera and Mono Basin, California, investigated with the SBAS-InSAR approach, Remote Sensing of Environment, 108, 277-289, 2007.
Trabelsi, N., Triki, I., Hentati, I., and Zairi, M.: Aquifer vulnerability and seawater intrusion risk using GALDIT, GQI SWI and GIS: case of a coastal aquifer in Tunisia, Environmental Earth Sciences, 75, 669, 2016.
Vapnik, V.: The Nature of Statistical Learning Theory· 6·[MJ New York, Springer-Verlag, 1, 995, 1995.
Vogel, R. M. and Fennessey, N. M.: Flow-duration curves. I: New interpretation and confidence intervals, Journal of Water Resources Planning and Management, 120, 485-504, 1994.
Walker, R., Gans, P., Allen, M., Jackson, J., Khatib, M., Marsh, N., and Zarrinkoub, M.: Late Cenozoic volcanism and rates of active faulting in eastern Iran, Geophysical Journal International, 177, 783-805, 2009.
Walker, R. and Jackson, J.: Active tectonics and late Cenozoic strain distribution in central and eastern Iran, Tectonics, 23, 2004.
World Bank: Islamic Republic of Iran: Cost Assessment of Environmental Degradation, Rural Development, Water and Environment Department32043-IR, 2005.
Wright, T. J., Parsons, B. E., and Lu, Z.: Toward mapping surface deformation in three dimensions using InSAR, Geophysical Research Letters, 31, 2004.

758 Yadav, M., Wagener, T., and Gupta, H.: Regionalization of constraints on expected watershed response behavior for
759 improved predictions in ungauged basins, Advances in water resources, 30, 1756-1774, 2007.
760 Yunjun, Z., Fattahi, H., and Amelung, F.: Small baseline InSAR time series analysis: Unwrapping error correction
761 and noise reduction, Computers & Geosciences, 133, 104331, 2019.
762